

An operational retrieval algorithm for determining aerosol optical properties in the ultraviolet

Thomas E. Taylor,¹ Tristan S. L'Ecuyer,² James R. Slusser,¹ Graeme L. Stephens,² and Christian D. Goering²

Received 15 March 2007; revised 14 September 2007; accepted 12 November 2007; published 2 February 2008.

[1] This paper describes a number of practical considerations concerning the optimization and operational implementation of an algorithm used to characterize the optical properties of aerosols across part of the ultraviolet (UV) spectrum. The algorithm estimates values of aerosol optical depth (AOD) and aerosol single scattering albedo (SSA) at seven wavelengths in the UV, as well as total column ozone (TOC) and wavelength-independent asymmetry factor (g) using direct and diffuse irradiances measured with a UV multifilter rotating shadowband radiometer (UV-MFRSR). A novel method for cloud screening the irradiance data set is introduced, as well as several improvements and optimizations to the retrieval scheme which yield a more realistic physical model for the inversion and increase the efficiency of the algorithm. Introduction of a wavelength-dependent retrieval error budget generated from rigorous forward model analysis as well as broadened covariances on the a priori values of AOD, SSA and g and tightened covariances of TOC allows sufficient retrieval sensitivity and resolution to obtain unique solutions of aerosol optical properties as demonstrated by synthetic retrievals. Analysis of a cloud screened data set (May 2003) from Panther Junction, Texas, demonstrates that the algorithm produces realistic values of the optical properties that compare favorably with pseudo-independent methods for AOD, TOC and calculated Ångström exponents. Retrieval errors of all parameters (except TOC) are shown to be negatively correlated to AOD, while the Shannon information content is positively correlated, indicating that retrieval skill improves with increasing atmospheric turbidity. When implemented operationally on more than thirty instruments in the Ultraviolet Monitoring and Research Program's (UVMRP) network, this retrieval algorithm will provide a comprehensive and internally consistent climatology of ground-based aerosol properties in the UV spectral range that can be used for both validation of satellite measurements as well as regional aerosol and ultraviolet transmission studies.

Citation: Taylor, T. E., T. S. L'Ecuyer, J. R. Slusser, G. L. Stephens, and C. D. Goering (2008), An operational retrieval algorithm for determining aerosol optical properties in the ultraviolet, *J. Geophys. Res.*, 113, D03201, doi:10.1029/2007JD008661.

1. Introduction

[2] The Earth's atmosphere contains many types of aerosols with various origins, each displaying its own unique set of chemical, physical and optical properties [Seinfeld and Pandis, 1998]. Changes in the concentrations of aerosols, either natural or anthropogenic, can lead to a wide variety of effects at various scales, ranging from the impairment of local and regional air quality due to forest fires [McMeeking *et al.*, 2005], to global changes in the stratospheric ozone shield [Farman *et al.*, 1985]. Research has convincingly

shown that changes in the global abundances of aerosols, generally due to anthropogenic forcing, lead to complicated climate feedback scenarios through direct and indirect effects [Nakajima *et al.*, 2001; Suzuki *et al.*, 2004] that may mask other sources of change in the Earth's climate such as those due to increases in greenhouse gases. Optically, aerosols can be classified as either absorbing, such as black carbons which heat the atmosphere and cool the surface, or as reflecting, such as sulfates and nitrates, which cool both the atmosphere and surface [Chung and Seinfeld, 2005]. These two aerosol types therefore cause radiative climate forcing of opposing sign, and both have nearly the same magnitude as that estimated due to CO₂ [Houghton *et al.*, 2001], highlighting the importance of carefully characterizing aerosol variations in time and space. It has further been conjectured that aerosols may significantly impact the radiative properties of clouds, an effect that could lead to a weakening of the Earth's hydrological cycle [Ramanathan

¹U.S. Department of Agriculture UV-B Monitoring and Research Program, Natural Resource Ecology Laboratory, Colorado State University, Fort Collins, Colorado, USA.

²Department of Atmospheric Science, Colorado State University, Fort Collins, Colorado, USA.

et al., 2001], which would produce further complications in determining sources of climate change.

[3] Although much of the research pertaining to the optical properties of aerosols has been focused on the visible region of the solar spectrum, scientists have recently begun to explore more intensely the interaction of aerosols with UV radiation. Although the UV spectral band (10 nm to 400 nm) comprises less than 10% of the solar radiant energy at the top of the atmosphere, it is of paramount importance to the Earth's climate as well as generating potentially serious biological and medical implications [Frederick *et al.*, 1989; Grant and Slusser, 2003; Kimlin *et al.*, 2003]. However, it is difficult to accurately characterize the amount of UV radiation that reaches the Earth's surface [Bernhard and Seckmeyer, 1999] because of the many factors which affect its transmission through the atmosphere, most notably variations in clouds [Kylling *et al.*, 1997], aerosols [Lorente *et al.*, 1994; Kylling *et al.*, 1998; Reuder and Schwander, 1999], and ozone [Slusser *et al.*, 1999; Fioletov *et al.*, 1997].

[4] A key ambition of the United States Department of Agriculture's (USDA) UltraViolet Monitoring and Research Program (UVMRP) is to improve knowledge of the UV transmission properties in cloud-free, turbid atmospheres from measurements made by ultraviolet multifilter shadow-band radiometers (UV-MFRSR). The UV-MFRSR, and its predecessor, the Vis-MFRSR, both designed and produced by Yankee Environmental Systems, Inc. (www.yesinc.com), are robust and stable instruments [Michalsky *et al.*, 1988] that have been employed in many research campaigns related to aerosol retrievals [e.g., McArthur *et al.*, 2003; Petters *et al.*, 2003; Wetzel *et al.*, 2003; Kassianov *et al.*, 2005; Kassianov *et al.*, 2007], since it has been shown that significant information pertaining to both the absorption and scattering by aerosol is contained in the combination of the direct and diffuse radiation component [Herman *et al.*, 1975]. The UVMRP network consists of approximately 34 automated UV-MFRSRs distributed in a grid-like pattern across the United States [Bigelow *et al.*, 1998]. After appropriate cloud screening the measured irradiances can be used as inputs into a Bayesian retrieval algorithm such as that described by Goering *et al.* [2005] to provide estimates of aerosol optical depth (AOD, at seven wavelengths), aerosol single scattering albedo (SSA, at seven wavelengths), total ozone column (TOC) and a wavelength-independent asymmetry factor (g), where the later has been added as an improvement to the new version of the algorithm along with the addition of wavelength correlations in AOD and SSA, which allows for the retrieval of more parameters than measurements.

[5] Although the retrieval framework introduced by Goering *et al.* [2005] showed promising retrievals of TOC and aerosol properties, many important questions were left unresolved and many improvements were required in order for the code to be used operationally. The primary objectives of this research are to characterize the error in the algorithm through sensitivity testing and optimization of the forward model, as discussed in section 2, introduction of a new cloud screening technique in section 3 and characterization of the behavior of the retrieval through synthetic retrievals as described in section 4. Analysis of the results from a single UVMRP site, discussed in section 5, indicates that the new approach yields more realistic results than the

original algorithm and is now well suited to be applied operationally across the UVMRP network.

2. Algorithm

[6] Following Goering *et al.* [2005], estimates of AOD, SSA, TOC and g with associated error covariances can be derived from direct and diffuse irradiance measurements via the optimal estimation (OE) technique which minimizes the cost function;

$$\Phi = (\mathbf{y} - \mathbf{F}(\hat{\mathbf{x}}))^T \mathbf{S}_y^{-1} (\mathbf{y} - \mathbf{F}(\hat{\mathbf{x}})) + (\hat{\mathbf{x}} - \mathbf{x}_a)^T \mathbf{S}_a^{-1} (\hat{\mathbf{x}} - \mathbf{x}_a), \quad (1)$$

by iteration of the Gauss-Newtonian equation,

$$\hat{\mathbf{x}} = \hat{\mathbf{x}}_{i-1} + \hat{\mathbf{S}} \left[\mathbf{K}^T \mathbf{S}_y^{-1} (\mathbf{y} - \mathbf{F}(\hat{\mathbf{x}}_{i-1})) + \mathbf{S}_a^{-1} (\mathbf{x}_a - \hat{\mathbf{x}}_{i-1}) \right], \quad (2)$$

with uncertainties given by,

$$\hat{\mathbf{S}} = \left(\mathbf{S}_a^{-1} + \mathbf{K}^T \mathbf{S}_y^{-1} \mathbf{K} \right)^{-1}. \quad (3)$$

[7] Here, $\hat{\mathbf{x}}$ represents the estimated values of the unknown state parameters, \mathbf{y} contains the measurements and \mathbf{x}_a represents any prior knowledge of the state parameters. Critical to the success of the OE approach, is the accurate specification of the a priori as well as the model-measurement error covariances, \mathbf{S}_a and \mathbf{S}_y , respectively, and a representative forward model, $\mathbf{F}(\mathbf{x})$, that characterizes the dependence of the measurements on the retrieval parameters and defines the Jacobian matrix, $\mathbf{K}_{ij} = \frac{\partial F_i(\mathbf{x})}{\partial x_j}$ [L'Ecuyer *et al.*, 2006]. In this work version 4.2 of the Tropospheric Ultraviolet-Visible (TUV) model was used, which focuses on the transmission of UV and visible in the troposphere by allowing variation of the most influential parameters such as ozone, gas and aerosol extinction as well as vertical profiles of atmospheric state variables like temperature and air density [Madronich, 1993].

2.1. Prior Information

[8] This section considers the problems of assigning appropriate error covariances and optimizing the forward model, both of which are critical to operational implementation of the algorithm described by Goering *et al.* [2005] but were not addressed in that study. The OE technique estimates values of the state parameters by combining the information contained in the measurements via the forward model with previous knowledge of the parameters via a priori values. A key feature of this approach is the fact that it is possible to retrieve a larger number of parameters than the number of available measurements because of the additional information provided by the a priori state vector and the ability to specify correlations between the retrieval parameters through the a priori error covariance matrix, \mathbf{S}_a . To this effect correlations are imposed on AOD and SSA as an exponential function of wavelength, consistent with values reported in current literature [e.g., Wenny *et al.*, 1998, 2001; Wetzel *et al.*, 2003; Petters *et al.*, 2003], via the off-diagonal elements of \mathbf{S}_a . This reduces the number of independent variables that need to be retrieved and provides more realistic estimates of the state parameters. The values

Table 1. Values of a Priori and Corresponding Standard Deviations for Each Retrieval Parameter Type

	A Priori Value	σ (Cloud Screening)	σ (Retrieval)
AOD (all λ)	0.80	0.27	0.50
SSA (all λ)	0.85	0.05	0.10
g	0.70	0.10	0.15
TOC	$\overline{\text{TOC}}_{\text{daily}}$	$2\%\overline{\text{TOC}}_{\text{daily}}$	$2\%\overline{\text{TOC}}_{\text{daily}}$

of a priori and standard deviations (σ) for each parameter used in the present study are shown in Table 1, selected to accurately encapsulate the expected range found in nature as estimated from values reported in the current literature (see above references). While the a priori values and standard deviations for AOD and SSA remain static in the code, as in the original algorithm, the new version employs dynamic values for TOC that are based on the daily mean TOC calculated from the UV-MFRSR data set via the direct sun technique [Gao *et al.*, 2001]. The static value of asymmetry factor formerly set in TUV (0.70) was adopted as the new a priori, with a standard deviation of 0.15, providing a 1- σ range of 0.55 to 0.85.

2.2. Measurement and Model Uncertainties

[9] The ultraviolet multifilter shadowband radiometer (UV-MFRSR) is similar in design to the visible spectrum version described by Harrison *et al.* [1994], and uses a plane horizontal diffuser and a rotating shadow band to make total sky and diffuse horizontal measurements in terms of detector voltages. The direct component of radiation is calculated via subtraction of the measured signals after removal of the dark count bias and correction for the plane horizontal detector's deviation from perfect cosine angular response. The direct and diffuse irradiances used in the retrieval algorithm are measured by the UV-MFRSR at seven wavelength channels in the UV spectrum; 300, 305, 311, 317, 325, 332 and 368 nm, each with a nominal bandpass of 2 nm. Measurements are made every 20 s and averaged into 3 min bins, which typically provides several hundred measurements per day at a site, depending on the latitude and Julian day.

[10] Wavelength-dependent estimates of measurement uncertainties are adopted from Krotkov *et al.* [2005a], which include contributions from quantization of the analog signal, dark bias, temperature dependence, angular response and shadowing corrections of the detector. Although these

uncertainties have been shown to depend on optical depth and SZA, the dependence is slight, so for simplicity a single conservative value of 3% is chosen to represent all conditions in the S_y error covariance matrix as shown in the top row of Table 2. When the signal-to-noise ratio (SNR) is small, which can occur at large solar zenith angles or at the lower wavelength channels because of the strong absorption by ozone, the information contained in the measurements is reduced, thereby resulting in ill-conditioned retrievals on which the algorithm is typically unable to converge to a solution. Cases in which this occurs are rejected via the cloud screening technique that is discussed in section 3. In order to convert measured voltages into irradiances, calibration for absolute spectral responsivity of the instrument filters, based on the Langley technique of Slusser *et al.* [2000] is used, introducing an additional source of measurement uncertainty, reported in the second row of Table 2.

[11] Beyond uncertainties in the measurements there are several important physical parameters used in the forward model that must be accounted for in the S_y error covariance matrix. A good discussion of the important parameters affecting calculations made by TUV is given by Lefer *et al.* [2003]. To this effect a clear-sky sensitivity study of TUV, similar to that performed by Schwander *et al.* [1997] using the System for Transfer of Atmospheric Radiation (STAR) radiative transfer model was conducted to determine the component of S_y due to uncertainties in the forward model. Potential errors from the assumption of g , surface pressure (p_s), surface albedo (α_s), temperature profile (T), column amount of sulfur dioxide (SO_2) and nitrogen dioxide (NO_2) are considered using the ranges of the variables defined in Table 3. Note that the range and increment of each variable used in the sensitivity testing was judiciously selected as a compromise to provide both a realistically broad subspace in order to demonstrate the physics of the model while at the same time limiting the computational and analysis requirements. In no way does the selection of parameter ranges and increments used in this study limit or control the state space in which the retrieval algorithm can perform effectively.

[12] Of all the parameters tested in this study, the modeled diffuse irradiances, $F(\mathbf{x})$, exhibit the strongest sensitivity to the asymmetry factor, g , which corresponds to the first moment of the phase function and represents the directionality of scattering with values of +1 (−1) indicating complete forward (back) scattering [Liou, 2002]. Although g is an important parameter required in radiative transfer calcu-

Table 2. Percent Error in Calculated Direct (Diffuse) Irradiances Due to Uncertainties in Model Variables^a

	300 nm	305 nm	311 nm	317 nm	325 nm	332 nm	368 nm
δ_{meas}	3.0 (3.0)	3.0 (3.0)	3.0 (3.0)	3.0 (3.0)	3.0 (3.0)	3.0 (3.0)	3.0 (3.0)
δ_{Langley}	3.8 (3.8)	3.7 (3.7)	3.5 (3.5)	3.4 (3.4)	3.2 (3.2)	3.0 (3.0)	2.1 (2.1)
δ_{α}	−(1.0)	−(1.1)	−(1.2)	−(1.2)	−(1.2)	−(1.2)	−(1.1)
δ_T	2.9 (2.8)	1.9 (1.9)	1.2 (1.2)	0.7 (0.8)	0.4 (0.4)	0.1 (0.2)	0.0 (0.0)
δ_{SO_2}	2.8 (3.0)	1.6 (1.8)	0.9 (1.0)	0.4 (0.4)	0.0 (0.0)	0.0 (0.0)	0.0 (0.0)
δ_{NO_2}	0.3 (0.4)	0.4 (0.5)	0.5 (0.6)	0.6 (0.7)	0.7 (0.9)	0.9 (1.0)	1.4 (1.6)
δ_{radtran}	−(1.5)	−(0.6)	−(0.5)	−(0.5)	−(0.5)	−(0.6)	−(0.7)
δ_{ϵ}	3.1 (3.1)	2.3 (2.3)	2.1 (2.1)	2.0 (2.0)	2.0 (2.0)	2.0 (2.0)	2.0 (2.0)
RMS	7.1 (7.5)	5.9 (6.1)	5.3 (5.5)	5.1 (5.3)	4.9 (5.1)	4.8 (5.0)	4.4 (4.7)

^aAveraged over all points in the AOD-SSA-SZA domain. RMS values shown in the bottom row are used as diagonal elements in the S_y matrix.

Table 3. Range of Values and Increments of the Physical Parameters Used in the TUV Forward Model During Sensitivity Testing^a

Parameter	Minimum	Maximum	Increment	Number
AOD	0.1	2.0	0.21	10
SSA	0.65	0.95	0.033	10
SZA	25°	65°	20°	3
TOC	260 DU	300 DU	10 DU	5
g	0.6	0.9	0.05	7
p_s	900 mbar	980 mbar	40 mbar	3
α_s	$\pm 1.5\%$ [Doda and Green, 1981]		-	3
	λ -dependent values			
T	$\pm 1.5\%$ U.S. Standard profile		-	3
SO ₂	0.0 DU	1.0 DU	0.5 DU	3
NO ₂	0.1 DU	0.7 DU	0.3 DU	3

^aNote that AOD, SSA, TOC and g are retrieval parameters, SZA is determined by the time and location of the measurements, p_s is taken from colocated ancillary measurements, α_s varies by terrain type, while T, SO₂ and NO₂ are fixed in the forward model.

lations, its determination through direct measurement has proven to be quite elusive, such that it is generally inferred using the aerosol size distribution, refractive index and particle shape [Andrews *et al.*, 2006]. Since fractional differences in modeled diffuse irradiances due to perturbations in g relative to $g = 0.70$, summarized in Table 4, show sensitivity similar to those produced by changes in TOC of 10 to 20 DU when turbidity is high, modifications were made to the algorithm to allow explicit retrieval of a wavelength independent value of g to be used in TUV. Note that only a simple wavelength-independent value is retrieved since it was felt that retrieving g as a function of wavelength would lead to an unrealistically large number of degrees of freedom of the retrieval. Furthermore, more explicit knowledge concerning realistic values and variations in g would be required for use in \mathbf{x}_a and \mathbf{S}_a . Although it is possible to use some wavelength parameterization of g to calculate values for use in the forward model, similar to the parameterization of the spectral dependence of AOD via the Ångström exponent [Schuster *et al.*, 2006], no such parameterization is known by the authors at this time. As deduced from Table 4, errors in modeled diffuse irradiances due to perturbations of g approximately triple when AOD increases from 0.3 to 1.2, indicating an increase in model sensitivity, and hence better conditioning of the algorithm for retrieving accurate estimates of g as atmospheric turbidity increases.

[13] The parameter to which TUV was found to have the second highest sensitivity is the surface pressure (p_s), which is scaled to the 1976 annual mean U.S. standard column air density profile. Variations in p_s of 940 ± 40 mbar, a realistic range for the Panther Junction site which sits at an altitude of 670 m, yielded deviations of $\pm 10\%$ in the modeled irradiances at 25° SZA, with some dependence on wavelength. An improvement was made to the algorithm to ingest into the forward model surface pressure data from ancillary measurements made at all UVMRP sites that are assumed to be accurate to within ~ 1 – 2 mbar.

[14] After the asymmetry parameter and surface pressure, the surface albedo, α_s , represents the largest source of uncertainty in forward model calculations. To test the sensitivity of the TUV model to this parameter the work of Doda and Green [1980] and Doda and Green [1981] was used in which reflected irradiances over a variety of surfaces, including desert sand, pine forest, green farmland,

brown farmland and snow cover, at discrete points in the wavelength range 290 to 400 nm were used to define wavelength-dependent values of α_s for each terrain type. Perturbations to α_s of ± 0.015 , representing half the uncertainty given in the sensitivity analysis of Schwander *et al.* [1997] (since it is anticipated that the Doda and Green [1981] measurements are better constrained than the assumptions used there) yields a mean error of $\sim 1\%$ in diffuse irradiances when averaged over a wide range of AOD, SSA and SZA values (see Table 2). Thus, provided each instrument site can be classified into one of the four Doda and Green [1981] dry terrain types and the corresponding wavelength-dependent values of α_s adopted, this yields a suitable estimate of the uncertainty due to surface albedo assumptions. It should be noted, however, that the large uncertainty in the reflectivity of snow in the UV [Blumthaler and Ambach, 1988] can lead to much larger errors in the retrieval. Since many sites lie in areas that can experience snow cover, a methodology for identifying these scenes should ultimately be adopted. Fortunately, each site in the UVMRP network is equipped with a downward looking photometer that can be used for this purpose.

[15] Uncertainties in the vertical temperature profile as well as in the column amounts of nitrogen dioxide (NO₂) and sulfur dioxide (SO₂), both significant absorbers in the UV spectral range, were also considered. A perturbation of $\pm 1.5\%$ to the U.S. Standard temperature profile used in TUV revealed deviations in the modeled irradiances of about 2% for the direct and diffuse components at 300 nm and 25° SZA, increasing to about 4% at 65° SZA. In all cases the error decreases with increasing wavelength because of the $\frac{1}{\lambda^4}$ Rayleigh effect. Variation of NO₂ by 0.4 ± 0.3 DU, a range of values covering standard continental background

Table 4. Percent Error in Modeled Diffuse Irradiances Due to Variation in Asymmetry Factor Relative to $g = 0.70$, i.e., $(I_{(g=x)} - I_{(g=0.70)})/I_{(g=0.70)}$ ^a

AOD	$g = 0.60$	$g = 0.65$	$g = 0.70$	$g = 0.75$	$g = 0.80$	$g = 0.85$	$g = 0.90$
0.3	-2.7%	-1.2%	0.0%	+1.2%	+2.4%	+3.6%	+4.8%
1.2	-6.6%	-3.4%	0.0%	+3.4%	+7.1%	+11.0%	+15.2%

^aResults shown for two select values of AOD at 368 nm and SZA = 25° with all other model parameters held fixed.

levels to moderately polluted urban settings based on SCIAMACHY data [Cede *et al.*, 2006], yields irradiance errors of $\approx 0.2\%$ (0.4%) at 300 nm to $\approx 1.0\%$ (1.5%) at 368 nm for the direct (diffuse) components at SZA 25° due to the smoothly increasing absorption spectra of this gas which peaks in the visible. Similarly, varying SO_2 , a strong absorber at the lower UV wavelengths, by 0.5 ± 0.5 DU, following the 1 DU uncertainty suggested by Schwander *et al.* [1997], resulted in irradiance differences of 2% (3%) at 300 nm for the direct (diffuse) component at SZA 25° . For both gases the error in modeled irradiances for the direct component at each wavelength approximately doubled from SZA 25° to SZA 65° , but remained roughly constant for the diffuse component. It should be noted that the error values adopted here are averaged over SZA, therefore the error in the direct component will be underrepresented for large SZA and slightly over estimated when SZA is small. Furthermore, unless ancillary measurements of column amounts of these gases are available, the adopted TUV settings for NO_2 and SO_2 are likely to be too low in heavily polluted atmospheres, yielding higher errors in modeled irradiances.

[16] Finally, it should be noted that additional errors in modeling UV irradiances can arise from the vertical profiles of humidity, ozone and molecular absorption coefficients. To account for these remaining error sources that are more difficult to quantify in a general way, an additional uncertainty of 2.0% at all wavelengths plus estimated wavelength-dependent uncertainties taken from Schwander *et al.* [1997] for the vertical ozone and aerosol extinction profiles is included in S_y . Each of the error sources studied here is summarized in Table 2. Assuming random and independent errors, the combined uncertainty that accounts for all error sources can be defined as the square root of the sum of the squares of the individual uncertainties;

$$\delta = \sqrt{\sum_{i=1}^8 (\delta_i)^2}, \quad (4)$$

where “i” ranges over all error sources in Table 2 which includes an additional source accounting for the approximation used to solve the equation of radiative transfer.

[17] The resulting RMS errors in the model-measurement as a function of wavelength for the snow free scenario, shown in the bottom row of Table 2, provide the necessary inputs for the diagonal elements in the S_y covariance error matrix used in the retrieval algorithm. For simplicity no correlations between channels (off-diagonals) are included in S_y since a technique for determination of these values has yet to be determined.

2.3. Forward Model and Retrieval Optimization

[18] In order for the algorithm to be implemented operationally on the more than 30 sites in the UVMRP network, the speed of the forward model and retrieval algorithm must be optimized. Mechanisms for achieving significant reductions in retrieval run time, without sacrificing retrieval accuracy, include increasing the speed of a single forward model calculation, reducing the number of forward model calculations required per iteration, and reducing the number of retrieval iterations required to achieve a solution. Each of

these features is considered in detail in Appendix A, while only key results are presented here for brevity.

[19] An order of 2 times increase in speed is achieved, with modest loss in accuracy (see Figure A1 in Appendix A), by adopting as the radiative transfer solver for use in the operational version of the algorithm the four stream version of the Discrete Ordinate Method (4-DOM) approximation, over the 8-DOM used by Goering *et al.* [2005]. Further time efficiency is gained by using the Delta-Eddington (Δ -Ed) approximation (>10 times faster than the 8-DOM) to provide a quick first step toward the solution on the first iteration of each retrieval. Changes were made to the calculation of the Jacobian matrix, \mathbf{K} , to reduce the total number of calls to the forward model, while the number of iterations required to achieve a solution has been reduced by using the previous estimate of the parameters as the first guess for the next scan rather than relying on the a priori values contained in \mathbf{x}_a . On the basis of these modifications the new version of the algorithm runs five to six times faster for a single iteration compared to the previous version discussed by Goering *et al.* [2005] and converges to a solution in about 25% fewer iterations.

[20] It is possible that the retrieval could be further optimized by employing precalculated look-up tables of modeled irradiances in lieu of on-the-fly radiative transfer calculations, similar to the technique used by Petters *et al.* [2003] for determining SSAs. However, determination of nonlinearities and the optimal resolution required for each state parameter, as well as quantifying the loss in accuracy are beyond the scope of the current study. Note that the OE algorithm discussed in this work allows simultaneous determination of all parameters contained in the state vector (AOD, SSA, TOC, g), with associated errors and diagnostics, in contrast to the other techniques cited in this work that focus on each parameter individually, e.g., Harrison and Michalsky [1994] for AOD, Petters *et al.* [2003] for SSA, Gao *et al.* [2001] for TOC, and typically have only a static error with no diagnostic outputs. More elaborate techniques using MFRSR data do exist however, such as that detailed by Kassianov *et al.* [2005] and Kassianov *et al.* [2007], which provides mean particle radius, total number concentration and imaginary refractive index via an iterative technique similar to that used by Petters *et al.* [2003]. Thus far, however, the Kassianov retrieval has been applied only to the visible part of the spectrum. Even more pertinent to the research described in this work is the relatively new technique introduced by Krotkov *et al.* [2005a] and Krotkov *et al.* [2005b], which determines unique values of single scattering albedo at each UV-MFRSR channel by constraining the forward model with ancillary inputs. Future work should certainly include an intercomparison with this technique.

3. Cloud Screening

[21] The presence of clouds in the field of view of the UV-MFRSR’s detector introduces systematic biases in aerosol retrievals that are too large to be adequately represented as an additional error source in S_y . This problem can be remedied by application of a cloud screening algorithm that removes cloud contaminated scenes. The work of Goering *et al.* [2005] used the cloud screening technique of Long

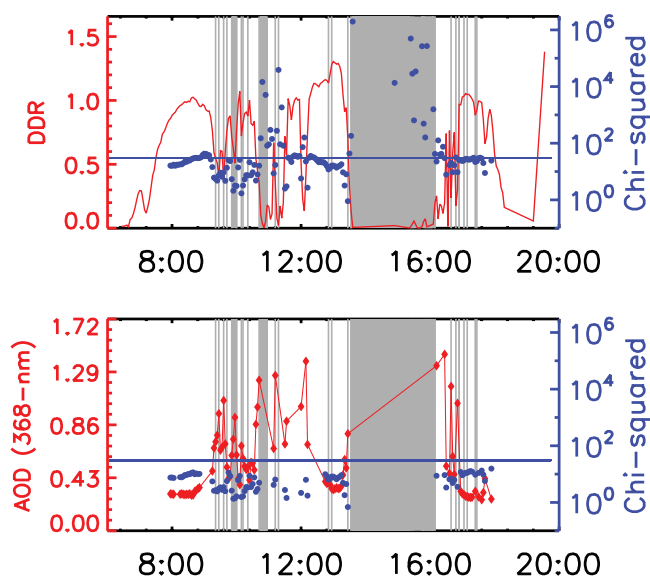


Figure 1. Time series plots for the χ^2 cloud screening algorithm testing for 24 May 2003 at Panther Junction, Texas. (top) Direct-to-diffuse irradiance ratios (DDR), plotted as a solid red line against the left ordinate, and χ^2 values, plotted as solid blue dots against a logarithmic right ordinate along with the upper boundary of the 98% confidence interval as a solid blue horizontal line. The gray shaded bars correspond to regions where at least three consecutive retrievals were determined to be cloudy by the Smirnov *et al.* [2000] routine. (bottom) Retrieval results based on the cloud-screened data set. The values of $\text{AOD}_{368\text{-nm}}$ are plotted as red diamonds with an interconnecting line against the left ordinate. The right ordinate shows χ^2 values determined from the operational retrieval, and again, the gray bars indicate regions determined cloudy by the Smirnov technique.

and Ackerman [2000], modified to operate on data collected from a Vis-MFRSR that was colocated at the Mexico City site. In this work we introduce an alternative “internally consistent” cloud screening method that is useful in the absence of ancillary broadband radiometer or Vis-MFRSR data, as it relies on the χ^2 statistic, a diagnostic output from the OE algorithm. In the context of the OE retrieval, in which Gaussian statistics are assumed, the value of χ^2 quantifies the statistical significance of a solution vector belonging to a predetermined state space. A retrieval is performed using the computationally fast two-stream Delta-Eddington ($\Delta\text{-Ed}$) approximation to the radiative transfer equation [Toon *et al.*, 1989] and the scan is rejected if the resulting χ^2 value falls above the 98% confidence interval, as determined from a χ^2 distribution table, since the presence of clouds in the detector field of view generally violates the assumed error characteristics, therefore causing values of χ^2 to exceed the value appropriate for the 16 degrees of freedom in the retrieval vector. For cases of extreme contamination the retrieval often fails to converge altogether, providing an alternate indication that the measurements do not fit the forward model assumptions and should therefore be screened. For retrievals that return χ^2 values lower than the 98% threshold ($\chi^2 < 30.6$ for $n-1 =$

15), the scene is taken to be cloud free and to have a sufficient signal-to-noise ratio (SNR), such that the measurements can subsequently be processed via the slower, but more accurate, operational version of the retrieval to provide estimates of the state parameters.

[22] The accuracy of the new χ^2 technique was analyzed by comparing results to another commonly used cloud screening algorithm introduced by Smirnov *et al.* [2000] that uses a series of tests contingent on the standard deviation and temporal consistency of $\text{AOD}_{500\text{-nm}}$, but which was modified for this application to use $\text{AOD}_{368\text{-nm}}$ calculated from the UV-MFRSR irradiance measurements via Langley extrapolation [Harrison and Michalsky, 1994]. Note that using Langley calculated values of AOD to perform cloud screening in the context of this research is somewhat circular, as AODs are parameters to be estimated by the retrieval algorithm, a strong argument for using the internally consistent $\Delta\text{-Ed}/\chi^2$ technique. To assess the agreement between the two screening methods a comparison of the $\Delta\text{-Ed}/\chi^2$ versus the Smirnov *et al.* [2000] AOD technique for the 6231 scans measured on 24 May 2003 at the Panther Junction site is shown in Figure 1. Although the linear correlation coefficient between χ^2 and DDR is not very strong ($R = -0.14$), in general it is apparent that for values of the direct-to-diffuse ratio (DDR) near zero (small direct, large diffuse component) χ^2 values become very large or do not exist because of unsuccessful convergence, while for large DDR, the values of χ^2 are near or below the 98% significance level. The gray shaded bars in Figure 1, which correspond to at least three consecutive scans that were determined to be cloudy by the Smirnov *et al.* [2000] routine, tend to exist wherever the χ^2 values are very high or where the χ^2 values do not exist because of nonconvergence of the algorithm. Figure 1 (bottom) shows the OE retrieved values of $\text{AOD}_{368\text{-nm}}$ for the scans that passed as clear sky along with the new χ^2 value calculated by the operational retrieval.

[23] Cloud screening results from the complete month of May, summarized in Table 5, show that 65.7% of the time the two techniques agree that the scans are either cloudy (30.9%) or cloud-free (34.8%). Situations in which the two methods disagree are represented by n_2 and n_3 in Table 5, indicating that 11.1% of the scans were accepted by the Smirnov *et al.* [2000] AOD technique but rejected by the $\Delta\text{-Ed}/\chi^2$ technique, while 23.2% of the scans exhibit the converse situation. The imbalance in these numbers suggests that the lower rejection rate of the $\Delta\text{-Ed}/\chi^2$ technique allows useful retrievals during the “borderline” cloud contamination scenes, such as might occur in the presence of thin cirrus. If desired, these scans could always be subsequently eliminated by postprocessing using a technique similar to Smirnov *et al.* [2000]. However, the new χ^2 -based screening provides a useful first cut at removing cloudy scenes that avoids the computational cost of processing these scans using the full algorithm. Overall, the results qualitatively indicate that the Delta-Eddington approximation, in conjunction with the χ^2 statistic, does in fact provide a fast, reasonably robust methodology for cloud screening that does not rely on ancillary measurements which may not always be available at the UVMRP operational sites. Note that a more thorough comparison with the technique of Long and Ackerman [2000], as was used by

Table 5. Comparison of the $\Delta\text{-Ed}/\chi^2$ Cloud Screening Technique With the Technique of Smirnov *et al.* [2000] for 6231 Scans From May 2003 at Panther Junction, Texas^a

	Smirnov Cloudy	Smirnov Clear
$\Delta\text{-Ed}/\chi^2$ cloudy	$n_1 = 1928$ (30.9%)	$n_2 = 691$ (11.1%)
$\Delta\text{-Ed}/\chi^2$ clear	$n_3 = 1444$ (23.2%)	$n_4 = 2168$ (34.8%)

^aThe number of cases in which both methods agree that the scene is cloudy (clear) are given as n_1 (n_4). Cases considered clear by the Smirnov technique but cloudy by the $\Delta\text{-Ed}/\chi^2$ technique fall into the n_2 category, while cases determined clear by $\Delta\text{-Ed}/\chi^2$ and cloudy by Smirnov are represented as n_3 .

Goering *et al.* [2005], should be performed in future research in order to provide further validation of the new $\Delta\text{-Ed}/\chi^2$ technique.

4. Synthetic Retrievals

[24] Synthetic retrievals provide a powerful tool for understanding the limitations imposed by assumptions made in any retrieval framework, allowing determination of the atmospheric conditions during which the algorithm provides accurate estimates of the unknown state parameters. For technical details concerning the synthetic retrievals the reader is referred to Appendix B while only a discussion of the results is given here. To characterize the quality of each synthetic retrieval the percent fractional difference between the retrieved and the “true” value of a parameter is used, i.e., $\Delta = \frac{\text{retrieved} - \text{truth}}{\text{truth}} \times 100$, while the RMS value, combining results of all sixteen retrieved parameters, provides a single quantification of the retrieval skill for each synthetic case. The estimated retrieval error in each parameter (ϵ), given by equation (3), is also used in determining the quality of the retrieval, as well as the chi-squared statistic that was introduced in section 3.

[25] Analysis of a large number of synthetic cases indicates the complex interaction between the state parameters as can be gleaned from careful consideration of Tables 6, 7, and 8, which show the “truth” and retrieved values of each state parameter along with the values of Δ and ϵ for the six cases introduced in Appendix B at 25° SZA. All of these cases have values of χ^2 less than the cutoff value of 30.6 for the 98% significance level, indicating that they would pass through the cloud screening (see discussion in section 3). Although it is challenging to definitively describe the behavior of the retrieval based on these results, in general Tables 6, 7, and 8 indicate that the quality of the retrieval improves (lower Δ and ϵ) with increasing “truth” values of AOD, as can be seen by comparing individual or RMS values for cases 1A, 2A and 3A, or cases 1B, 2B and 3B in Tables 6, 7, and 8, each of which uses increasing values for “truth” AOD. Disregarding cases 1A and 1B (Table 6), which contain the lower values of “truth” AOD, it can be seen that the retrieval of AOD and SSA at wavelengths 317 nm and greater is better than about 1.5%, i.e., $\Delta < 1.5$. Another noticeable trend is the strong decrease in retrieval skill of TOC and asymmetry factor when the “truth” values of SSA and g are lowered as can be observed by comparison of case 2A to 2B and 3A to 3B. The misestimation of TOC in turn affects the retrieval of AOD and SSA at the lower wavelengths because of loss in the SNR where absorption by ozone is strong.

[26] Results from a single synthetic retrieval are highlighted in Figure 2 for case 2A as defined in the left hand portion of Table 7. This scenario, in which “truth” AOD is near the a priori value and SSA and g are significantly larger than a priori shows that the retrieval provides reliable estimates of all of the parameters. In contrast Figure 3 shows that for case 2B (right hand portion of Table 7), in which SSA and g are significantly lower than the a priori, the retrieval of g is high by 14% and the retrieval of TOC is high by about 10%, which strongly affects the retrieval of AOD and SSA at the lower wavelengths. Even in this case the retrieval of AOD and SSA at wavelengths 317 nm and larger is better than 1.5%, as previously stated.

[27] From the synthetic retrieval results it was found to be beneficial to constrain the retrieval using the DS TOC from the Gao *et al.* [2001] technique as previously discussed. Another improvement was made by widening the a priori range via the variances in S_a from the original values adopted by Goering *et al.* [2005] to increase the ability of the retrieval to return statistically significant results when the state parameters have real values that exist in the tail of the Gaussian distribution, especially for very low values of AOD. This doubling of the a priori range allows for significant retrievals ($\chi^2 < 30.6$) of AOD down to about 0.045 and as high as about 2.0. This indicates that the algorithm is able to converge on a solution and provide a reasonable estimate of AOD ($\Delta < 10\%$, except for 300 nm) in pristine environments, although the estimated errors from \hat{S} are of order 50% and the retrieved values for SSA and g are essentially the a priori values. It is worth noting that the minimum retrieved value of AOD found here is similar to the minimum reported in other UV-MFRSR studies, while the maximum values would most likely exist only during cloudy conditions or during extreme events such as caused by smoke. For example, Wenny *et al.* [2001] reported a range of AOD_{368-nm} from 0.030 to 1.2 at Black Rock Mountain in North Carolina, while corresponding ranges in central Alaska are 0.15 to 0.25 for a spring marine air mass, 0.11 to 0.14 for a spring Asian air mass, and 0.05 to 0.06 for both a summer and spring Arctic air mass [Wetzel *et al.*, 2003]. Therefore the retrieval algorithm will be able to provide rough estimates of background AOD at the UVMRP sites with pristine environments, such as in Alaska and Montana but will provide the most useful information during more turbid conditions that routinely exist at most sites. However, it is possible to tune the algorithm for retrieving very low values of AOD by changing the constraints induced via the a priori and a priori covariances and perhaps by using a more accurate version of the radiative transfer approximation during these conditions.

[28] Although it might be expected that the retrieval will perform poorly as the SZA increases because of a loss in the SNR, synthetic retrievals indicate that the skill in determining the state parameters is unaffected by increasing air mass at SZAs of 45° and 65°. In fact, lower values of DDR at larger SZA suggest that the measurements actually contain more information because of the increase in the diffuse component of radiation caused by a larger number of photon scattering events. Eventually however, when the attenuation of the radiation is very large because of thick air mass (SZA > 70°), the increase of information in the measurements is not enough to overcome the loss in SNR

Table 6. Summary of Two Synthetic Retrieval Cases Showing the Values of Each of the Sixteen Retrieval Parameters Used for “Truth” and the Retrieved Values, as Well as the Percent Difference (Δ) Between “Truth” and Retrieved and the Retrieval Error (ϵ) Determined From Equation (3)^a

	Case 1A				Case 1B			
	“Truth”	Retrieved	Δ , %	ϵ , %	“Truth”	Retrieved	Δ , %	ϵ , %
AOD ₃₀₀	0.150	0.175	16.4	26.5	0.150	0.114	−23.8	38.5
AOD ₃₀₅	0.140	0.152	8.6	19.5	0.140	0.124	−11.4	23.5
AOD ₃₁₁	0.130	0.135	3.5	16.7	0.130	0.125	−3.9	18.2
AOD ₃₁₇	0.120	0.123	2.2	16.8	0.120	0.118	−1.5	17.4
AOD ₃₂₅	0.110	0.111	1.2	17.7	0.110	0.110	−0.2	17.9
AOD ₃₃₂	0.100	0.102	2.0	18.5	0.100	0.101	1.3	18.9
AOD ₃₆₈	0.090	0.094	4.7	18.2	0.090	0.089	−1.2	19.6
SSA ₃₀₀	0.900	0.839	−6.7	11.8	0.700	0.847	21.1	11.7
SSA ₃₀₅	0.910	0.854	−6.1	10.9	0.710	0.829	16.8	11.3
SSA ₃₁₁	0.920	0.878	−4.5	9.4	0.720	0.804	11.6	10.3
SSA ₃₁₇	0.930	0.890	−4.3	8.9	0.730	0.795	8.9	10.0
SSA ₃₂₅	0.940	0.900	−4.2	8.9	0.740	0.798	7.8	10.0
SSA ₃₃₂	0.950	0.899	−5.4	9.1	0.750	0.805	7.3	9.9
SSA ₃₆₈	0.960	0.900	−6.2	8.9	0.760	0.802	5.6	9.8
TOC	290.0	287.7	−0.8	1.5	290.0	294.1	1.4	1.4
<i>g</i>	0.850	0.770	−9.41	18.0	0.500	0.630	26.0	22.6
RMS	—	—	6.5	13.8	—	—	12.4	15.7
χ^2	—	9.8	—	—	—	10.4	—	—

^aAlso shown are the percent RMS Δ , ϵ and χ^2 values used to quantify the skill of the retrieval as discussed in the text.

and the retrieval produces results with unacceptably low skill and high error. The threshold SZA will of course vary with latitude and Julian day.

5. Application to Data From Panther Junction, Texas

[29] The retrieval as described here has been applied to UV-MFRSR data collected at a UVMRP site in Big Bend National Park, Panther Junction, Texas, located in the southwestern region of the state (29.130°N, 103.51°W,

Table 7. Summary of Two Synthetic Retrieval Cases as in Table 6 but Using Moderate “Truth” Values of AOD^a

	Case 2A				Case 2B			
	“Truth”	Retrieved	Δ , %	ϵ , %	“Truth”	Retrieved	Δ , %	ϵ , %
AOD ₃₀₀	0.900	0.949	5.4	11.5	0.900	0.751	−16.6	13.0
AOD ₃₀₅	0.880	0.902	2.5	6.3	0.880	0.813	−7.6	6.3
AOD ₃₁₁	0.860	0.869	1.1	3.7	0.860	0.832	−3.3	3.6
AOD ₃₁₇	0.840	0.844	0.5	2.7	0.840	0.829	−1.3	2.7
AOD ₃₂₅	0.820	0.821	0.1	2.5	0.820	0.818	−0.3	2.5
AOD ₃₃₂	0.800	0.801	0.1	2.4	0.800	0.801	0.1	2.4
AOD ₃₆₈	0.780	0.780	0.1	2.3	0.780	0.781	0.1	2.3
SSA ₃₀₀	0.900	0.854	−5.1	10.8	0.700	0.836	19.4	11.0
SSA ₃₀₅	0.910	0.884	−2.9	6.9	0.710	0.779	9.8	7.7
SSA ₃₁₁	0.920	0.912	−0.9	4.1	0.720	0.741	3.0	5.1
SSA ₃₁₇	0.930	0.926	−0.5	3.6	0.730	0.736	0.9	4.6
SSA ₃₂₅	0.940	0.940	0.0	3.4	0.740	0.737	−0.4	4.4
SSA ₃₃₂	0.950	0.949	−0.2	3.4	0.750	0.746	−0.5	4.4
SSA ₃₆₈	0.960	0.959	−0.1	3.7	0.760	0.753	−1.0	4.3
TOC	290.0	284.8	−1.8	4.2	290.0	305.9	5.5	3.5
<i>g</i>	0.850	0.840	−1.2	15.9	0.500	0.570	14.0	24.2
RMS	—	—	2.2	5.5	—	—	8.1	6.4
χ^2	—	3.9	—	—	—	5.1	—	—

^aThese are the same cases that are highlighted in the text and in Figures 2 and 3.

Table 8. Summary of Two Synthetic Retrieval Cases as in Tables 6 and 7 but Using Relatively Large “Truth” Values of AOD

	Case 3A				Case 3B			
	“Truth”	Retrieved	Δ , %	ϵ , %	“Truth”	Retrieved	Δ , %	ϵ , %
AOD ₃₀₀	1.600	1.596	−0.25	9.8	1.600	1.320	−17.5	10.6
AOD ₃₀₅	1.580	1.579	−0.1	5.1	1.580	1.455	−7.9	5.0
AOD ₃₁₁	1.560	1.559	−0.1	2.6	1.560	1.506	−3.5	2.6
AOD ₃₁₇	1.540	1.537	−0.2	1.7	1.540	1.517	−1.5	1.6
AOD ₃₂₅	1.520	1.520	0.0	1.4	1.520	1.512	−0.5	1.4
AOD ₃₃₂	1.500	1.499	−0.1	1.3	1.500	1.498	−0.1	1.3
AOD ₃₆₈	1.480	1.481	0.1	1.2	1.480	1.479	0.0	1.2
SSA ₃₀₀	0.900	0.900	0.1	9.7	0.700	0.854	22.1	10.2
SSA ₃₀₅	0.910	0.910	0.0	5.6	0.710	0.781	10.0	6.4
SSA ₃₁₁	0.920	0.920	0.0	3.4	0.720	0.741	3.0	4.3
SSA ₃₁₇	0.930	0.929	−0.1	2.9	0.730	0.734	0.6	3.9
SSA ₃₂₅	0.940	0.941	0.01	2.8	0.740	0.734	−0.8	3.8
SSA ₃₃₂	0.950	0.948	−0.2	2.8	0.750	0.742	−1.1	3.8
SSA ₃₆₈	0.960	0.959	−0.1	2.9	0.760	0.750	−1.3	3.8
TOC	290.0	290.1	0.5	6.1	290.0	319.7	10.2	5.0
<i>g</i>	0.850	0.850	0.0	15.9	0.500	0.560	12.0	23.9
RMS	—	—	0.1	4.7	—	—	8.5	5.6
χ^2	—	13.2	—	—	—	12.9	—	—

670 m elevation). This remote park is part of the Chihuahuan Desert, and in spite of its isolation from major industrial or urban centers, has been ranked among those with the poorest visibility in the western half of the U.S. park system [Hand et al., 2002; Schichtel et al., 2006], allowing a chance to test the OE retrievals ability to resolve varying levels of turbidity and aerosol types.

5.1. Retrieval Parameters and Error

[30] A cloud screened data set was produced using the algorithm described in section 3 and estimates of AOD, SSA, TOC and *g* were made using the new operational version of the algorithm. Values of Angstrom exponent (α), which can be used to parameterize the wavelength dependence of the AOD were then calculated, as will be discussed below. Monthly time series of AOD_{368-nm}, SSA_{368-nm}, TOC, asymmetry factor and calculated Angstrom exponent are shown in Figure 4 (left), while the corresponding retrieval errors determined from \hat{S} (equation (3)) are shown in Figure 4 (right), along with the χ^2 significance values in the fifth panel in Figure 4 (right). Note that values of AOD and SSA at all channels other than 368 nm are omitted here for brevity, and that in general, retrieval results are best at the longer wavelengths as was demonstrated by Goering et al. [2005], because of the strong attenuation of radiation by ozone at the lower wavelengths. Only linear correlation coefficients (*R*) are used in the statistical analysis.

[31] Overall the results confirm that errors in all parameters, except TOC, decrease with increasing AOD, indicating atmospheric turbidity is the primary source of information driving the retrieval. The daily fluctuations in AOD_{368-nm} (Figure 4, first panel) cover a range of 0.08 to 1.52 with a negatively correlated error (*R* = −0.78) ranging from about 34% down to about 2%, while the values of SSA_{368-nm} (Figure 4, second panel) range from about 0.74 to 1.00 with mean monthly error of 6% negatively correlated to AOD_{368-nm} (*R* = −0.81). The variations in TOC (Figure 4, third panel) range from about 265 to 330 DU,

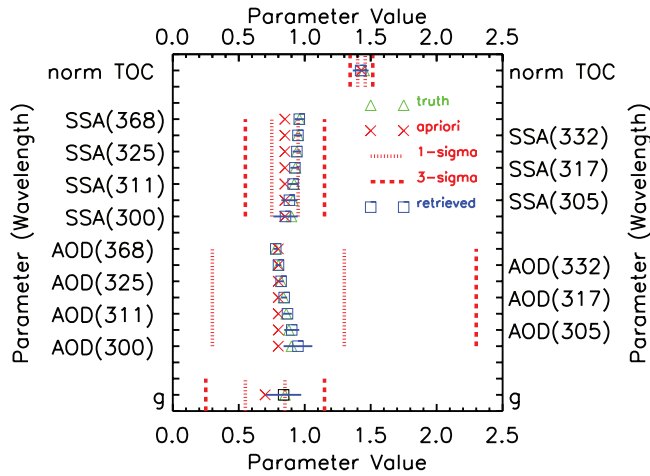


Figure 2. Results from a single synthetic retrieval (case 2A in Table 7) performed at local noon ($\text{SZA} = 14.4^\circ$) at Panther Junction, Texas, on 22 May, showing the a priori (red crosses), “truth” (green triangles) and retrieved values with horizontal error bars (blue squares). The 1- and 3- σ deviations from the a priori are plotted as red dotted and dashed lines, respectively. The ordinate labels indicate the atmospheric parameter with values plotted against the abscissa. The TOC shown here is normalized ($\text{TOC}/200$), as is done in the retrieval, such that all parameters have values of the same order of magnitude. For this particular case the retrieved values of all parameters are close to the “truth” values, as quantified by the relatively small values of Δ and $\text{RMS } \Delta$ shown in Table 7.

with an error ranging between 1 and 8% with monthly mean of 3.6%. Interestingly, constraint of the TOC using the direct sun (DS) values from the *Gao et al.* [2001] technique, as opposed to retrieving it from a much broader annual climatology, yields a much weaker correlation with $\text{AOD}_{368\text{-nm}}$ as well as a broader range of retrieved values. Unless increases in TOC are assumed to coincide with increases in AOD, as might occur during tropospheric pollution events for example, this can be considered an improvement to the algorithm as it suggests decoupling of two unrelated variables. Accurate retrieval of this parameter is imperative in order to retrieve aerosol properties at the lowest wavelength channels where the attenuation of radiation is very sensitive to ozone absorption in the Huggins bands. The values of asymmetry factor, shown in the fourth panel of Figure 4, range from 0.54 to 0.98 with a monthly mean error 17% which is negatively correlated with $\text{AOD}_{368\text{-nm}}$ ($R = -0.64$), indicating more reliable retrieval results during high atmospheric turbidity conditions. As mentioned in section 2.2 the inclusion of g as an explicitly retrieved variable removes the need to represent it in the S_y matrix and allows the model some flexibility rather than relying on a fixed value for all situations. Recall that larger values of g indicate an increase in the forward scattering of the phase function, as is expected from larger sized particles such as desert dust, which has been shown to have $g \simeq 0.9$ in the UV [*Madronich, 1993*].

[32] The fifth panel in Figure 4 (left) shows the time series of the Ångström exponents (with 2σ outliers removed) calculated as,

$$\alpha = \frac{\ln\left(\frac{\text{AOD}_1}{\text{AOD}_2}\right)}{\ln\left(\frac{\lambda_2}{\lambda_1}\right)}, \quad (5)$$

which is derived by taking the ratio of the expression,

$$\text{AOD} = \beta_t \lambda^{-\alpha}, \quad (6)$$

at two wavelengths [*Stephens, 1994*]. Although the derived value of α is dependent on the choice of wavelength due to spectral curvature [*Schuster et al., 2006*], in this work α are obtained using $\text{AOD}_{332\text{-nm}}$ and $\text{AOD}_{368\text{-nm}}$ as the estimated retrieval error is smallest at these longer wavelengths. Positive values of α indicate inverse wavelength dependence of AOD and larger α , which indicate stronger dependence on wavelength, are associated with smaller aerosol particles. The direction of the wavelength dependence in AOD indicated by the positive values of α in Figure 4 agrees with values reported in the current literature [e.g., *Kylling et al., 1998; Wetzel et al., 2003*], while the fluctuations in α suggest a variation in the size of the aerosol particles, as will be examined more closely in the following sections.

5.2. Retrieval Diagnostics

[33] Several critical diagnostics are built into the OE retrieval framework as discussed fully by *Rodgers* [2000], allowing for interpretation of the absolute behavior and accuracy, as well as relative comparisons between retrievals. The first diagnostic, the a priori–matrix (A-matrix) quantifies the use of the a priori information in each retrieval. The A-matrix diagonals represent the fractional weighting of the retrieval’s reliance on the measurements versus the a priori values (1 = total reliance on the measurements, 0 = total

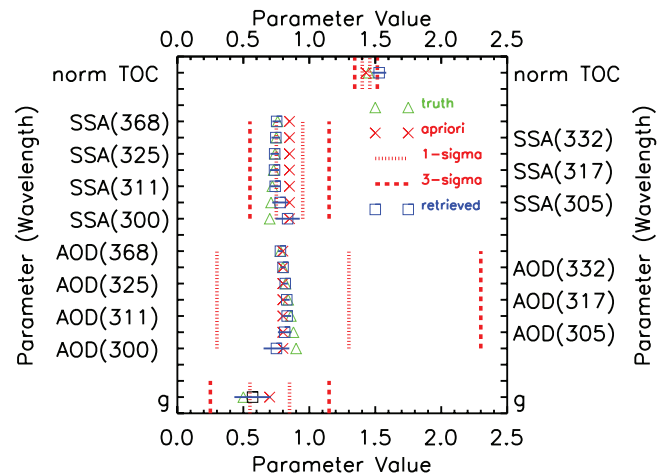


Figure 3. Same as Figure 2 except for case 2B in Table 7, which uses the same values of “truth” AOD but smaller values of SSA and g . Note the larger differences between “truth” and retrieved values in this case compared to Figure 2.

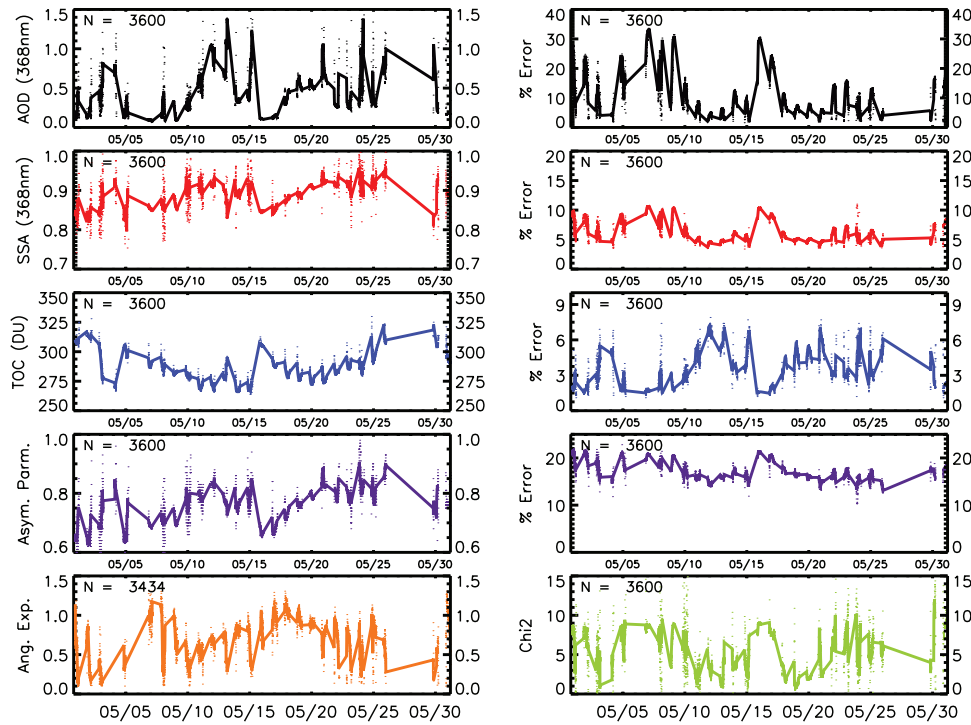


Figure 4. Retrieval results for May 2003 at Panther Junction, Texas, using the new operational version of the algorithm. (left) Time series of $AOD_{368\text{-nm}}$ (first panel), $SSA_{368\text{-nm}}$ (second panel), TOC (third panel), asymmetry factor (fourth panel) and Angstrom exponent calculated with equation (5) using 332 and 368 nm (fifth panel), each with a 30 point (90 min) running mean overplotted as a solid line. (right) Corresponding time series of retrieval error in estimated values of $AOD_{368\text{-nm}}$ (first panel), $SSA_{368\text{-nm}}$ (second panel), TOC (third panel) and asymmetry factor (fourth panel) as calculated from equation (3). The χ^2 significance values are shown in the fifth panel on the right. Note the data shown here has been screened at the 98% confidence interval, i.e., $\chi^2 < 30.6$.

reliance on the a priori), since each solution for each retrieval parameter is a linear combination of the a priori value and the value derived from the model-measurements. The second diagnostic, the Shannon information content (H), provides a measure of the reduction in the size of the solution space relative to the a priori space, given in terms of bits of information. Another diagnostic, as was discussed by Goering *et al.* [2005, section 2.3], are the various degrees of freedom (dof), which quantify the amount of information available in the model and measurements through eigenvalue analysis of the Jacobian matrix, \mathbf{K} . The standard measures of dof are given by the dof_s and dof_m , which indicate the number of independent measurements available, the effective rank of the problem in measurement space, and the number of independent parameters which can be determined from the measurements, the effective rank of the problem in state space, respectively. Another measure of dof is given by the dof_a , calculated as the trace of the \mathbf{S}_a matrix, which indicates the number of independent parameters that need to be retrieved, a value that decreases as correlations are imposed in \mathbf{S}_a via off-diagonal elements as was discussed in section 2.1. Note, however that this value remains constant ($dof_a = 13.9$ in this study) once \mathbf{S}_a has been determined prior to running the retrieval. In this research the degrees of freedom ratio, given as $dof_R = dof_s/dof_a$ is introduced to provide a succinct measure of retrieval conditioning, indicating the ratio of the

number of independent parameters that need to be retrieved to the number of independent measurements that are available. An ideal retrieval contains exactly the same amount of information in the measurements as the number of independent retrieval parameters that are to be estimated such that $dof_R = 1$.

[34] The diagnostic parameters are presented in Figure 5. A-matrix values are always near 1 for both $AOD_{368\text{-nm}}$ and TOC indicating that the measurements are largely responsible for constraining these parameters. The A-matrix values for retrieved $SSA_{368\text{-nm}}$ cover the range 0.06 to 0.90 with a monthly mean of 0.66 and a positive correlation to error in 368-nm AOD ($R = 0.78$), indicating that the measurements provide more information to effectively constrain this parameter when turbidity is high because of the increase in the diffuse component of radiation, as will be shown later. The A-matrix values for the asymmetry factor range from 0.08 to 0.55 with a monthly mean = 0.25, again indicating that there is not enough information in the measurements to fully determine g , as has already been stated. The degrees of freedom for signal, dof_s , measurement, dof_m , and ratio, dof_R , all increase significantly with increasing $AOD_{368\text{-nm}}$, again confirming that the information contained in the measurements increases with turbidity. Values of dof_R are always less than one, however, highlighting the fact that the retrieval is always underconstrained, requiring some additional information to reach a solution, in this case supplied

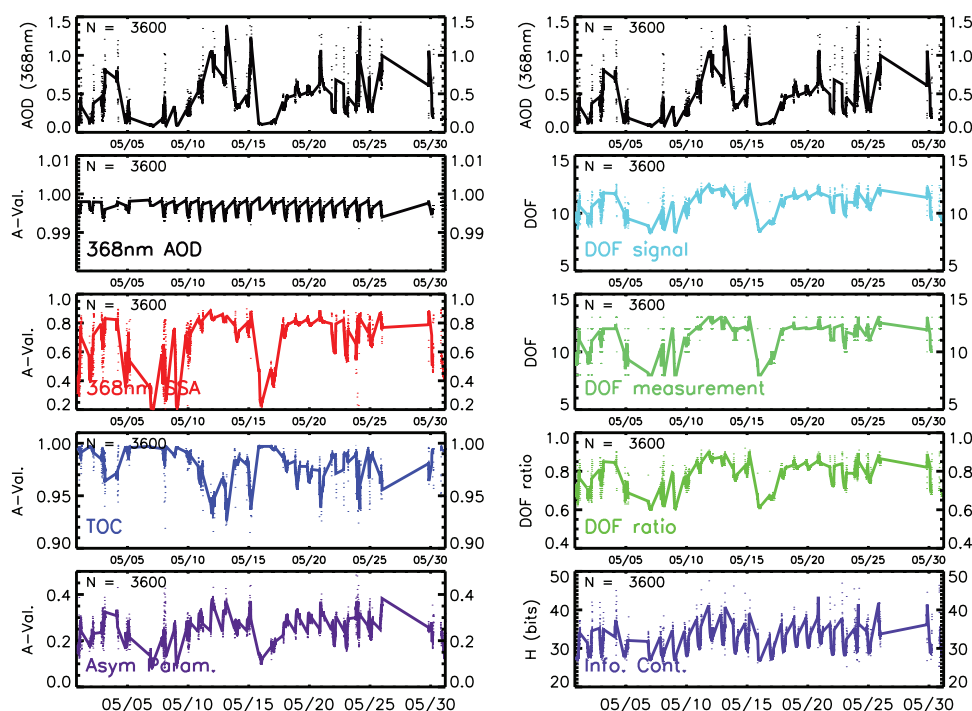


Figure 5. Diagnostic results corresponding to the retrieved values shown in Figure 4. (left) Retrieved values of $AOD_{368\text{-nm}}$ (first panel) for reference, followed by A-matrix values for $AOD_{368\text{-nm}}$, $SSA_{368\text{-nm}}$, TOC and asymmetry factor, respectively. (right) $AOD_{368\text{-nm}}$ (first panel) for reference, followed by values of degrees of freedom for signal (dof_s) and measurements (dof_m) and the dof ratio (dof_r), respectively, while values of the Shannon information content (H) are shown in the fifth panel.

by the a priori assumptions. It is worth noting, however, that this is not a result of the optimal estimation framework itself but rather an artifact of the underlying physics that govern radiative transfer through a turbid atmosphere. Other retrieval algorithms must also supply additional information whether explicitly or implicitly through assumptions about the dependence of optical depth and single scatter albedo on wavelength, for example. The fifth panel of Figure 5 shows that the values of the Shannon information content, H , are positively correlated to the values of $AOD_{368\text{-nm}}$ ($R = 0.67$), emphasizing the positive correlation between information contained in the measurements and atmospheric turbidity.

5.3. Diurnal Properties

[35] As mentioned previously the direct-to-diffuse ratio (DDR) of the measured irradiances, which is a strong function of both air mass and turbidity, can be used to parameterize the turbidity state of the atmosphere. Shown in Figure 6 are values of the direct, diffuse and total components of the UV-MFRSR measured irradiances at 368 nm and the DDR for 12 May (Figure 6, top) and 17 May (Figure 6, bottom) 2003. The DDR on 12 May shows that the diffuse component is twice that of the direct, indicating strong scattering as would be expected during times of high aerosol loading, while conversely, on 17 May the diffuse component is only about half that of the direct, as expected when the atmosphere is relatively aerosol free [Lorente *et al.*, 1994]. The smooth, bell shaped function of each component of radiation on both days, an artifact of the correlation between increasing air mass with SZA, is an

indicator that the sky was either cloud free or contained a layer that was more or less homogeneous all day long. The later case is unlikely however, since the total radiation has nearly the same value on both days, suggesting that the cloud screening algorithm has not merely allowed a cloudy day to pass undetected. Also of note is that the similarity in the total radiation on both days, regardless of the atmospheric turbidity, suggests that the aerosols tend to scatter significantly more radiation than they absorb, consistent with higher values of retrieved $SSA_{368\text{-nm}}$ on 12 May than on 17 May, as will be seen below.

[36] The diurnal properties of the retrieved parameters are illustrated in Figure 7, which shows daily time series of $AOD_{368\text{-nm}}$, $SSA_{368\text{-nm}}$, TOC, g and α for 12 May (Figure 7, left) and 17 May (Figure 7, right) 2003 at Panther Junction, Texas, along with S_x error and A-matrix values. The OE retrieved values of $AOD_{368\text{-nm}}$ (Figure 7, first panels) are overplotted with the UVMRP calculated values derived via the Langley method, indicating almost perfect agreement between the data sets on these days. A-matrix values near unity on both days indicate high reliance on the measurements for these retrievals, while the AOD error returned in S_x has a strong negative correlation with AOD, consistent with behavior suggested by synthetic retrievals.

[37] Shown in the second set of panels in Figure 7, differences in the daily mean retrieved values of $SSA_{368\text{-nm}}$ (≈ 0.92 on 12 May and ≈ 0.85 on 17 May) suggest variations in the scattering properties of the aerosols, although A-matrix values closer to 1 on the turbid day

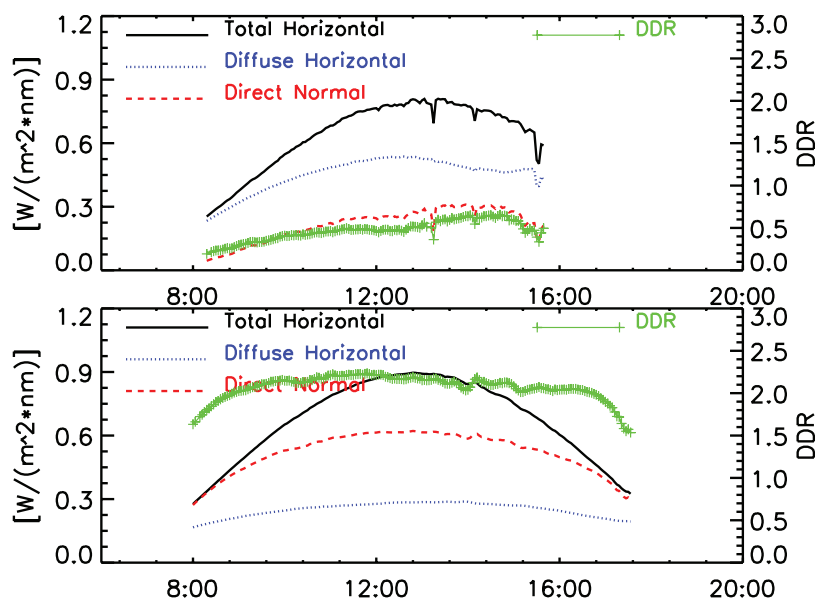


Figure 6. Daily time series plots of the UV-MFRSR measured irradiances on select days (top) 12 May and (bottom) 17 May 2003 from Panther Junction, Texas. The total horizontal (solid black curve), diffuse horizontal (dotted blue curve) and direct normal (dashed red curve) are plotted against the left ordinate, while the DDR (green crosses with solid line) is plotted against the right ordinate.

(12 May) indicate more information for retrieving SSA with decreasing DDR. The third set of panels in Figure 7 show that the TOC values derived from the Total Ozone Mapping Spectrometer (TOMS), the direct sun (DS) technique [Gao *et al.*, 2001] (which were used as the a priori) and the OE retrieved values all agree within uncertainties. The daily RMS difference between the OE and DS derived values is about 4 to 5 DU. Note that the monthly mean error ($\approx 3.6\%$) in OE retrieved TOC is about twice that of the claimed 2% error from the DS technique of Gao *et al.* [2001].

[38] Shown in the fourth panels of Figure 7 are the OE retrieved values of asymmetry factor, indicating that the running mean averages on the two days are significantly different. As was discussed in section 2.2, TUV is sensitive to changes in g , so allowing it to vary during the retrieval process is likely to reduce errors and yield more accurate retrievals of the other parameters, although the retrieved value of g itself may not be too useful because of its high uncertainty. Finally, the fifth panels in Figure 7 show the intercomparison between Ångström exponent from the Langley and OE derived AOD values, indicating very small RMS differences. The average values of 0.67 and 1.08 on 12 and 17 May, respectively, suggest larger aerosol size when turbidity is lower. In general, $\alpha > 2$ indicate small aerosol particles associated with combustion byproducts, while $\alpha < 1$ have been shown to correspond to larger particles such as sea salt and dust [Schuster *et al.*, 2006]. Although they are not expected to be the same in the UV spectral range, in the visible spectrum (415 to 860 nm) values of α near 2 were shown to correlate to accumulation mode particles, while values closer to zero were associated with Saharan dust during the BRAVO field campaign at a site near Panther Junction [Hand *et al.*, 2004].

[39] It is of some interest to more deeply investigate the dependence of the SSA on wavelength since it can vary depending on aerosol type, e.g., direct for large dust particles and inverse for black carbon [Bergstrom *et al.*, 2002], providing an indirect means for determination of the aerosol type present in the atmosphere. Although much of the previous research in the UV has shown a direct wavelength dependence [Petters *et al.*, 2003; Wetzel *et al.*, 2003], Goering *et al.* [2005] reported an inverse dependence in Mexico City. The time series plots of the retrieved values of SSA for all seven wavelength channels shown in Figure 8 for 12 May (Figure 8, top left) and 17 May (Figure 8, top right) indicate a more or less direct wavelength dependence in SSA on both days, especially for the longer wavelengths. The A-matrix values (Figure 8, bottom) indicate more information in the measurements for determining SSA on the turbid day at most channels, but a noticeably lower value at 300 nm, suggests that there is virtually no information available at this wavelength because of the strong absorption by ozone. Although it was speculated by Goering *et al.* [2005] that the presence of some unaccounted for absorbing aerosol or gas, such as NO_2 , was the culprit for the inverse wavelength dependence in that work, it is suggested here that the inverse wavelength dependence may have been an artifact of the coupling of a highly absorbing atmosphere at the heavily polluted Mexico City site and the retrieval returning values of the SSA that were progressively further from a priori values for increasing wavelengths because of the choice of an unrealistically tight variance for this parameter. In other words, the atmosphere at the time of the measurements may have contained a strongly absorbing aerosol (low SSA) but the retrieval was stuck near the a priori of 0.85 for the shorter wavelengths, while it returned values closer to “truth” for

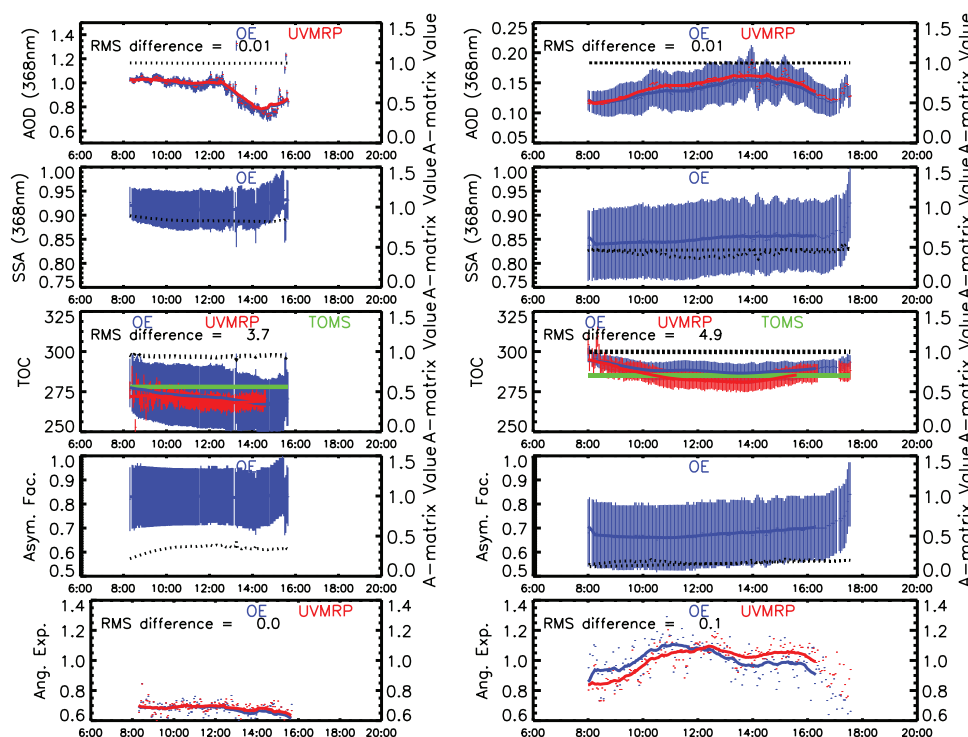


Figure 7. Retrieval results from (left) 12 May 2003 and (right) 17 May 2003 for Panther Junction, Texas. Plotted against the left ordinate in each panel are the values of $AOD_{368\text{-nm}}$ (first panel), $SSA_{368\text{-nm}}$ (second panel), TOC (third panel), asymmetry factor (fourth panel) and Ångström exponent calculated using 332 and 368 nm (fifth panel). Optimal estimation (OE) values are plotted in blue with vertical error bars, and independently determined values (where available) are plotted in red and green, with RMS differences between the data sets indicated. Note the difference in the range of the $AOD_{368\text{-nm}}$ ordinate scale for the two days. Plotted as black dotted lines against the right ordinate in each panel (except for Ångström exponent) are the A-matrix values, which indicate the fractional reliance of the retrieval on the measurements.

the longer wavelengths. More rigorous studies of this issue are required for ultimate clarification.

[40] In summary, all of the retrieval properties discussed in this section are self-consistent and agree well with values calculated using alternative techniques. Retrieval errors are generally negatively correlated with the values of $AOD_{368\text{-nm}}$, the dominant factor that has repeatedly been found to drive the information content of the measurements. The large spatial and temporal domain of the current UVMRP instrument network, and colocation with many heavily instrumented sites, e.g., Goddard, Maryland, and Mauna Loa, Hawaii, will allow for more comprehensive validation of the algorithm in the near future, especially comparison to data from the Aeronet network [Holben *et al.*, 1998] and to the newly introduced techniques of Krotkov [Krotkov *et al.*, 2005a; Krotkov *et al.*, 2005b] and Kassianov [Kassianov *et al.*, 2005; Kassianov *et al.*, 2007]. Ideally a more thorough intercomparison of data from the Panther Junction site should be performed with data collected from July to October 1999 in Big Bend National Park during the BRAVO campaign [see Schichtel *et al.*, 2006, and references therein]. Furthermore other special field campaigns, e.g., Mirage-Mex in Mexico City [Fast *et al.*, 2007, and references therein] and the Texas Air Quality Study in Houston (<http://www.tceq.state.tx.us/>

implementation/air/airmod/texaq-files/TexAQS_II.html) will allow continued validation and analysis for improvement of the OE retrieval algorithm described in this work.

6. Conclusions

[41] Many practical issues concerning a Bayesian optimal estimation (OE) algorithm for determining UV aerosol optical properties, including thorough forward model sensitivity testing and a new cloud screening method have been addressed. The OE technique described in this work offers the advantage of allowing explicit specification of uncertainties in measurements, forward model assumptions and any prior information used, provides estimates of the errors in all retrieval products and supplies a suite of diagnostics for assessing retrieval performance. Using uncertainties established through rigorous model sensitivity testing and optimization, the retrieval was shown to be well behaved and to provide accurate and useful results over a broad domain of atmospheric conditions as determined via synthetic retrievals. Constraining the value of TOC, based on the Gao *et al.* [2001] DS technique, as well as incorporation of the wavelength-independent asymmetry factor as an explicitly determined parameter and using the surface pressure from ancillary measurements in TUV, reduces the

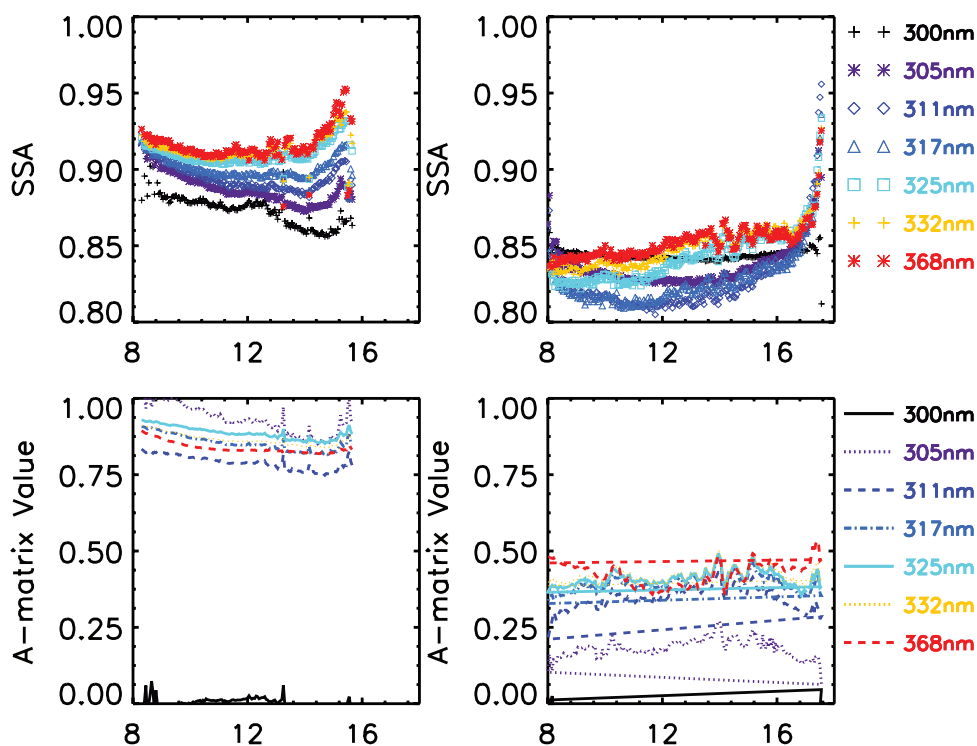


Figure 8. (top) Time series plots of the OE retrieved SSA values at seven wavelengths for (left) day 12 May and (right) day 17 May for Panther Junction, Texas. (bottom) Associated A-matrix values for the same two days. Note that values for the two days are plotted on a common scale for ease of comparison. The a priori value for SSA set in the retrieval was 0.85.

error in the radiative transfer calculations and allows for better estimations of the other parameters. Selection of the 4-DOM radiative transfer approximation used in the forward model, a more efficient scheme for calculating the Jacobian matrix, an improvement in the retrieval initialization method and a novel “internal” cloud screening method all optimize execution speed, with minimal sacrifice in accuracy.

[42] Synthetic retrievals were used to show that the skill in determining the state parameters improves strongly with increasing “truth” values of AOD and to a lesser extent with increasing “truth” values of SSA and g . When “truth” values of AOD are within about one standard deviation of the mean, as determined by the AOD a priori, the algorithm provides estimates of the state parameters within about 2% of the true values. The algorithm was shown to converge on a solution for AOD as low as 0.045, although the retrieved values of the other state parameters (SSA, TOC, g) were essentially equivalent to the a priori values in this case. The maximum value of AOD on which the algorithm was able to converge to a solution was shown to be about 2.0.

[43] Retrieved values of $\text{AOD}_{368\text{-nm}}$, $\text{SSA}_{368\text{-nm}}$, TOC and g , determined from the May 2003 data set at Panther Junction, Texas, show realistic variations in time with estimated retrieval error in AOD, SSA and g negatively correlated to the atmospheric turbidity, while the retrieval error in TOC is positively correlated to turbidity. The A-matrix values indicate that $\text{AOD}_{368\text{-nm}}$ and TOC are well determined by the measurements for all conditions, while the determination of $\text{SSA}_{368\text{-nm}}$ is reliant on the DDR as

controlled by the atmospheric turbidity and SZA. The retrieval of asymmetry factor, although it improves somewhat with increasing turbidity, is heavily reliant on the selected a priori value, but allows the model flexibility in determining the other parameters. Furthermore, the high positive correlation of dof_R and information content with $\text{AOD}_{368\text{-nm}}$ shows that the retrieval constraint and resolution increases with atmospheric turbidity. Detailed comparisons against pseudo-independent methods for $\text{AOD}_{368\text{-nm}}$, TOC and Ångström exponent indicate favorable and consistent results. Unfortunately, no independent measurements of SSA and g are available for direct comparison at this site and time period, so future work is needed for a complete validation of the technique.

[44] It is our intention to implement the algorithm operationally at each of the 34 sites in the UVMRP network, producing values of the aerosol optical properties in the UV spectral range, as well as total ozone column, each with estimated uncertainties, with next-day Web delivery made available to the public. Detailed information concerning the operational sites is available at the UVMRP web site; <http://uvb.nrel.colostate.edu/UVB>. This data will provide the most comprehensive and extensive ground-based UV aerosol climatology available in the continental United States. The availability of these aerosol products will allow thorough investigation and site to site intercomparisons by researchers who are interested in modeling atmospheric UV transmission and actinic fluxes, as well as those concerned with air quality and transport issues and the biological (health and agricultural) effects of UV exposure. Furthermore the

retrieval scheme could be further developed to provide information in the visible region of the spectrum using the same TUV forward model. However this would require a full sensitivity testing and the appropriate adjustment of the a priori and other variables, as well as a strong constraint or retrieval of the surface albedo, which is highly variable in the visible relative to the UV.

Appendix A: Algorithm Efficiency

[45] Since the retrieval algorithm discussed in this paper is meant to be incorporated in an operational manner, it is desirable to make the code as efficient as possible with little sacrifice in the accuracy of the retrieved values. This appendix addresses several issues related to the efficiency of the new operational algorithm.

[46] 1. Examining differences between the n-stream Discrete Ordinate Method (n-DOM) [Stamnes *et al.*, 1988], evaluated at 4, 8 and 32 streams, and the 2-stream Delta-Eddington (Δ -Ed) approximation [Toon *et al.*, 1989], both of which are radiative transfer solvers readily available within the TUV code shows that the 8-DOM, which was selected for use in the work performed by Goering *et al.* [2005] is 15 times faster than the 32-DOM and yields virtually identical irradiances over the entire AOD-SSA domain space for all wavelengths and SZA. In contrast, the Δ -Ed approximation is over 200 times faster than the 32-DOM, but yields large irradiance differences which are strong functions of wavelength, SZA and AOD. A reasonable compromise between the improvement in speed of the Δ -Ed and the high accuracy of the 8-DOM is provided by the 4-DOM approximation, which performs calculations about 30 times faster than the 32-DOM, while retaining reasonable accuracy under most atmospheric conditions. The fractional differences in diffuse irradiances (the direct component of irradiance is not a function of the number of streams), as a function of AOD and SSA with other variables held fixed, are shown in Figure A1 at 300 nm (Figure A1, left) and 368 nm (Figure A1, right), indicating very little error at SZA 25° (top row) and 45° (middle row) for all AOD, SSA and wavelengths. At SZA 65° (bottom row) the error dependence on AOD becomes somewhat pronounced at 300 nm, ranging from about 1% to 7%, but still shows little dependence on SSA. At 368 nm the error is smaller and flatter with AOD, ranging from about -2.4% to +2.5% over the domain. Since the 4-DOM approximation provides an ideal combination of accuracy and speed, it has been adopted for use in the operational version of the algorithm, while the Δ -Ed approximation is retained for the first iteration of the algorithm to provide a quick first step toward the solution. Furthermore, the Δ -Ed approximation coupled with the χ^2 statistic provides a novel means for cloud screening the irradiance data set as discussed in section 3. The components of S_y owing to choice of the 4-DOM radiative transfer solver are presented as $\delta_{radtran}$ in Table 2 and represent the mean values over all points in the AOD-SSA-SZA domain. As such, they will slightly overestimate the error at small SZA and low AOD and, conversely, underestimate the error at large SZA and high AOD, but these biases are expected to be small when compared to the magnitude of the combined uncertainty from all sources.

[47] 2. By far the most computationally expensive part of the retrieval algorithm is calculation of irradiances by the TUV forward model for the Jacobian matrix, \mathbf{K} . In the original version of the algorithm the rows of \mathbf{K} were calculated separately by evaluating the forward model once for each element of the state vector individually perturbed by 2%. However, the presence of sharply spiked weighting functions (rows of \mathbf{K}), indicates that perturbations to a single parameter at a specific wavelength has little effect on the modeled irradiances at the other wavelengths, thereby making it feasible to perturb all seven values of both AOD and SSA simultaneously rather than individually. This results in a fourfold reduction of radiative transfer calculations from 16 to 4 times per iteration, providing a substantial time savings, as a typical retrieval requires 2 to 4 iterations of equation (2) in order to converge to a solution. Testing showed that the algorithm runs 3.5 times faster for a 3 iteration retrieval because of this modification, while no perceptible changes to the individual elements of \mathbf{K} , and hence to the retrieved parameters or the diagnostic outputs, were observed.

[48] 3. Since the evaluation of $\mathbf{F}(\mathbf{x})$ and \mathbf{K} required during each iteration are computationally expensive, another significant increase in algorithm speed can be realized by reducing the number of iterations required to achieve a solution for each retrieval. This can be accomplished when dealing with data that is sequential in time or space by allowing the previous measurements to provide information about the state at the current time step. Many applications of the OE technique use the a priori values of the state parameters as the initial guess for the first iteration of the retrieval algorithm, i.e., $\hat{\mathbf{x}}_{0(n)} = \mathbf{x}_a$ for each new retrieval. However, since the values of the state parameters in consecutive measurements are typically strongly correlated because of the short temporal spacing of the UV-MFRSR measurements, it is reasonable to expect that retrieved AOD, SSA, TOC and g from a retrieval will provide a closer first guess for the subsequent scan than would the a priori values. This modification not only reduces the average number of iterations by $\approx 25\%$, but also improves convergence problems associated with large first steps that are often required when the a priori-derived initial first guess is far from the true solution.

[49] 4. A typical retrieval converges in two to four iterations using the new version of the algorithm, and it was found that retrievals which do not converge by about the fifth iteration are generally unable to converge even by iteration ten or greater, as is often the case when SZA > 65°. Five iterations is therefore used as the maximum number allowed to further optimize retrieval run time, and in the event that a retrieval is unable to converge on a solution, the subsequent retrieval is initialized with $\hat{\mathbf{x}}_{0(n)} = \mathbf{x}_a$ by default. This default is also used for the first retrieval of a new local day. It should be noted that, as discussed by Rodgers [2000, section 5.6.2], the values of the \mathbf{x}_a vector should never be updated on the basis of previous estimates obtained by the retrieval as this is equivalent to using the measurements more than once, a clear violation of the optimal estimation technique.

[50] 5. Error trapping corrections were written into the code to flag and correct cases when the retrieval returns unphysical estimates of various state parameters, which in

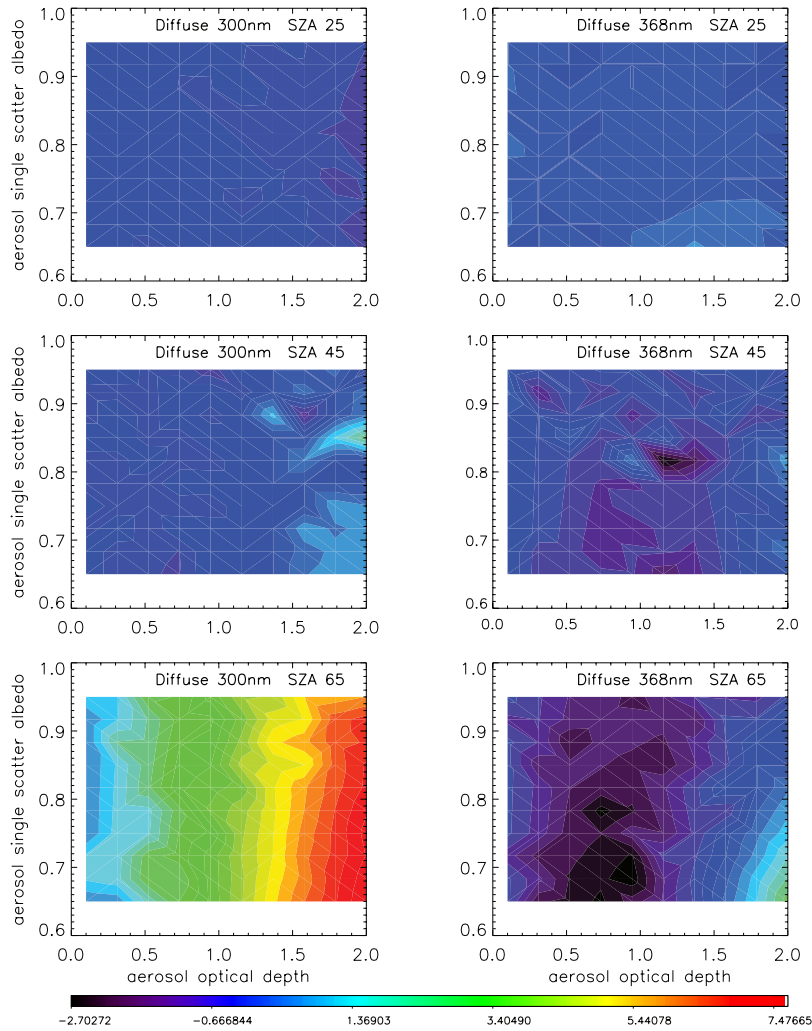


Figure A1. Percent differences in modeled irradiances between the 4-stream and the 32-stream Discrete Ordinate Method approximation used in the forward model. All plots are in AOD-SSA space with $\text{TOC} = 280$ DU, $g = 0.70$, $\alpha_s = 0.05$ and $p_s = 940$ mbar. (left) 300 nm and (right) 368 nm. (top) SZA 25° , (middle) SZA 45° and (bottom) SZA 65° . Scale ranges from -2.7% (black) to $+7.5\%$ (red), with purple corresponding to 0% and blue to $+1\%$.

turn cause the forward model to crash. Specifically, negative values of AOD are reassigned to 0.2, while values of SSA or g greater than one are reassigned to 0.995. This reassignment is performed only when unphysical values are returned on the first two iterations of the algorithm. If unphysical values are returned after the third iteration then the retrieval is considered to be unsuccessful and is aborted. This modification proved to be useful by allowing some scans to converge when large jumps in state space occurred, nudging the parameter into unphysical space, because of a first guess that is far from the final solution.

Appendix B: Synthetic Retrievals

[51] As a prelude to analyzing algorithm performance through synthetic retrievals, it was first demonstrated that the retrieval solution is well behaved and unimodal in state space by evaluation of the retrieval cost function (equation (1)) over a range of AOD, SSA, SZA and other state parameters. Contour plots of the cost function, as

shown for 368 nm and SZA 25° in Figure B1, verify that a unique global minimum exists for all UV-MFRSR channels and for SZA less than 65° , indicating that the information content of the measurements, or retrieval resolution, increases with both increasing SZA and atmospheric turbidity. Note however that a simultaneous drop in the signal-to-noise ratio (SNR) with increasing SZA limits the ability of the retrieval to converge on a solution beyond about 65° for the synthetic tests performed here.

[52] Synthetic retrievals provide a test bed for determining the ability of the algorithm to return accurate estimates of the state parameters and allow for verification of the limits of the retrieval. The tests are initialized by assigning realistic values of the atmospheric retrieval variables (AOD, SSA, TOC and g), referred to as the “truth” conditions. The “truth” values are then used as inputs to the forward model to calculate values of the irradiances, which act as a set of “synthetic” measurements to be used as inputs to the OE retrieval algorithm. Comparison of the retrieved state parameters to the “truth” values allows for quantification

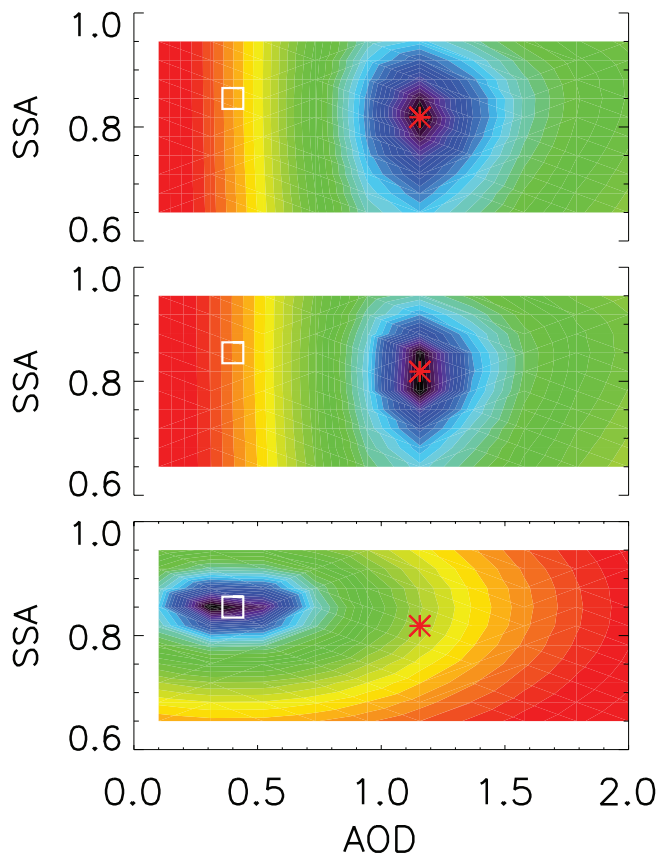


Figure B1. Contours of the scalar cost function (equation (1)) representing the retrieval solution space in the AOD-SSA domain at SZA 25° and wavelength 368 nm. (top) Total solution space, (middle) contribution to the solution from the measurements and (bottom) contribution to the solution from the a priori term. The white boxes represent the a priori values of AOD and SSA, while the red asterisk represent the “truth” values. AOD is labeled on the abscissa and SSA is labeled on the ordinate in all plots. The scale is arbitrary, but common to all three panels, and represented in logarithmic space to highlight the features of the contours. The smooth contours with the single minima indicated the well-behaved nature of this particular retrieval problem.

of the retrieval skill. In this work a series of six synthetic cases using three distinct regimes for “truth” values of AOD, and two distinct regimes for “truth” values of SSA and g were defined. In order to be physically consistent with results reported in the current literature when selecting “truth” conditions to be used in the synthetic retrievals, values of AOD in each case were assigned an inverse wavelength dependence while the values of SSA were assigned a direct wavelength dependence [e.g., *Wenny et al.*, 2001; *Wetzel et al.*, 2003; *Petters et al.*, 2003]. In all cases the “truth” TOC was assigned a value of 290 DU, which is very close to the average daily value of 286 DU for the test day, 22 May 2003 at Panther Junction, Texas, as calculated via the direct sun (DS) technique of *Gao et al.* [2001]. Tests were performed using three values of SZA (25° , 45° , 65°) to determine the approximate air mass at

which the signal-to-noise ratio becomes too small for the retrieval to successfully converge.

[53] The set of three atmospheric turbidity cases was defined by assigning values of AOD as: AOD_{low} ; $0.15 \rightarrow 0.09$ in -0.01 steps, AOD_{mod} ; $0.90 \rightarrow 0.78$ and AOD_{high} ; $1.60 \rightarrow 1.48$, both in -0.02 increments from 300 to 368 nm, where, for convenience of discussion, the three cases are labeled as low, mod and high, although these terms are completely subjective and used purely for reference in the following discussion. The set of two distinct regimes for SSA and g are; $\text{SSA} = 0.90 \rightarrow 0.96$ in 0.01 increments from 300 to 368 nm with $g = 0.85$ and $\text{SSA} = 0.70 \rightarrow 0.76$ in 0.01 increments from 300 to 368 nm with $g = 0.50$. Results from these synthetic cases are discussed in section 4 and summarized in Tables 6, 7, and 8 and Figures 2 and 3.

[54] **Acknowledgments.** This research was supported under the NOAA Cooperative agreement NA17RJ1228, by the Office of Biological and Environmental Research of the U.S. Department of Energy (DE-FG02-94ER61748) as part of the Atmospheric Radiation Measurement Program, and by USDA/CSREES grant 2004-34263-14270-Amendment 1. We would like to thank three anonymous reviewers for their well-thought-out comments. Thanks to Chris Kummerow, John Volckens, John Davis, Nick Krotkov and Denis O’Brien for their discussion and comments regarding this work. We would also like to thank the staff at the UVMRP for providing the data from the UV-MFRSR instrument as well as invaluable computer services. The TUV model was provided courtesy of Sasha Madronich of NCAR, Boulder, Colorado.

References

- Andrews, E., et al. (2006), Comparison of methods for deriving aerosol asymmetry parameter, *J. Geophys. Res.*, *111*, D05S04, doi:10.1029/2004JD005734.
- Bergstrom, R. W., P. B. Russell, and P. Hignett (2002), Wavelength dependence of the absorption of black carbon particles: Predictions and results from the TARFOX experiment and implications for the aerosol single scattering albedo, *J. Atmos. Sci.*, *59*, 567–577.
- Bernhard, G., and G. Seckmeyer (1999), Uncertainty of measurements of spectral solar UV irradiance, *J. Geophys. Res.*, *104*(D12), 14,321–14,345.
- Bigelow, D., J. Slusser, A. Beaubien, and J. Gibson (1998), The USDA ultraviolet radiation monitoring program, *Bull. Am. Meteorol. Soc.*, *79*, 601–615.
- Blumthaler, M., and W. Ambach (1988), Solar UVB-albedo of various surfaces, *Photochem. Photobiol.*, *48*(1), 85–88.
- Cede, A., J. Herman, A. Richter, N. Krotkov, and J. Burrows (2006), Measurements of nitrogen dioxide total column amounts using a Brewer double spectrophotometer in direct Sun mode, *J. Geophys. Res.*, *111*, D05304, doi:10.1029/2005JD006585.
- Chung, S. H., and J. H. Seinfeld (2005), Climate response of direct radiative forcing of anthropogenic black carbon, *J. Geophys. Res.*, *110*, D11102, doi:10.1029/2004JD005441.
- Doda, D., and A. Green (1980), Surface reflectance measurements in the UV from an airborne platform, Part 1, *Appl. Opt.*, *19*(13), 2140–2145.
- Doda, D., and A. Green (1981), Surface reflectance measurements in the UV from an airborne platform, Part 2, *Appl. Opt.*, *20*(4), 636–642.
- Farman, J., B. Gardiner, and J. Shanklin (1985), Large losses of total ozone in Antarctica reveal seasonal ClO_x/NO_x interaction, *Nature*, *315*, 207–210.
- Fast, J., et al. (2007), A meteorological overview of the MILAGRO field campaigns, *Atmos. Chem. Phys.*, *7*, 2233–2257.
- Fioletov, V. E., J. B. Kerr, and D. I. Wardle (1997), The relationship between total ozone and spectral UV irradiance from Brewer observations and its use for derivation of total ozone from UV measurements, *Geophys. Res. Lett.*, *24*(23), 2997–3000.
- Frederick, J., H. Snell, and E. Haywood (1989), Solar ultraviolet radiation at the Earth’s surface, *Photochem. Photobiol.*, *51*, 443–450.
- Gao, W., J. Slusser, J. Gibson, G. Scott, D. Bigelow, J. Kerr, and B. McArthur (2001), Direct-sun column ozone retrieval by the ultraviolet multifilter rotating shadow-band radiometer and comparison with those from Brewer and Dobson spectrophotometers, *Appl. Opt.*, *40*(19), 3149–3155.
- Goering, C. D., T. S. L’Ecuyer, G. L. Stephens, J. R. Slusser, G. Scott, J. Davis, J. C. Barnard, and S. Madronich (2005), Simultaneous retrievals of column ozone and aerosol optical properties from direct and diffuse

- solar irradiance measurements, *J. Geophys. Res.*, **110**, D05204, doi:10.1029/2004JD005330.
- Grant, R., and J. Slusser (2003), Spatial variability in UV radiation during the growing season across the continental USA, *Theor. Appl. Climatol.*, **74**, 167–177.
- Hand, J., S. Kreidenweis, D. E. Sherman, J. Collett, S. Hering, D. Day, and W. Malm (2002), Aerosol size distributions and visibility estimates during the Big Bend Regional Aerosol and Visibility Observational (BRAVO) study, *Atmos. Environ.*, **36**, 5043–5055.
- Hand, J., S. Kreidenweis, J. Slusser, and G. Scott (2004), Comparison of aerosol optical properties derived from sun photometry to estimates inferred from surface measurements in Big Bend National Park, Texas, *Atmos. Environ.*, **38**, 6813–6821.
- Harrison, L., and J. Michalsky (1994), Objective algorithm for the retrieval of optical depths from ground-based measurements, *Appl. Opt.*, **33**(22), 5126–5132.
- Harrison, L., J. Michalsky, and J. Berndt (1994), Automated multifilter rotating shadow-band radiometer: An instrument for optical depth and radiation measurements, *Appl. Opt.*, **33**(22), 5118–5125.
- Herman, B., R. Browning, and J. DeLuisi (1975), Determination of the effective imaginary term of the complex refractive index of atmospheric dust by remote sensing: The diffuse-direct radiation method, *J. Atmos. Sci.*, **32**, 918–925.
- Holben, B., et al. (1998), AERONET—A federated instrument network and data archive for aerosol characterization, *Remote Sens. Environ.*, **66**, 1–16.
- Houghton, J., Y. Ding, D. Griggs, M. Noguer, P. van der Linden, X. Dai, K. Maskell, and C. Johnson (2001), *Climate Change 2001: The Scientific Basis—Contribution of Working Group I to the Third Assessment Report of the Intergovernmental Report on Climate Change*, Cambridge Univ. Press, Cambridge, U. K.
- Kassianov, E. I., J. C. Barnard, and T. P. Ackerman (2005), Retrieval of aerosol microphysical properties using surface MultiFilter Rotating Shadowband Radiometer (MFRSR) data: Modeling and observations, *J. Geophys. Res.*, **110**, D09201, doi:10.1029/2004JD005337.
- Kassianov, E. I., C. M. Flynn, T. P. Ackerman, and J. C. Barnard (2007), Aerosol single-scattering albedo and asymmetry parameter from MFRSR observations during the ARM aerosol IOP 2003, *Atmos. Chem. Phys.*, **7**, 3341–3351.
- Kimlin, M., N. Downs, and A. Parisi (2003), Comparison of human facial UV exposure at high and low latitudes and the potential impact on dermal vitamin D production, *Photochem. Photobiol. Sci.*, **2**, 370–375.
- Krotkov, N., P. K. Bhartia, J. Herman, J. Slusser, G. Labow, G. Scott, G. Janson, T. F. Eck, and B. Holben (2005a), Aerosol ultraviolet absorption experiment (2002 to 2004), part 1: Ultraviolet multifilter rotating shadowband radiometer calibration and intercomparison with CIMEL sunphotometers, *Opt. Eng.*, **44**(4), 041004.
- Krotkov, N., et al. (2005b), Aerosol ultraviolet absorption experiment (2002 to 2004), part 2: Absorption optical thickness, refractive index, and single scatter albedo, *Opt. Eng.*, **44**(4), 041005.
- Kylling, A., A. Albold, and G. Seckmeyer (1997), Transmittance of a cloud is wavelength-dependent in the UV-range: Physical interpretation, *Geophys. Res. Lett.*, **24**(4), 397–400.
- Kylling, A., A. Bais, M. Blumthaler, J. Schreder, C. Zerefos, and E. Kosmidis (1998), Effect of aerosols on solar UV irradiances during the photochemical activity and solar ultraviolet radiation campaign, *J. Geophys. Res.*, **103**(D20), 26,051–26,060.
- L'Ecuyer, T., P. Gabriel, K. Leesman, S. J. Cooper, and G. L. Stephens (2006), Objective assessment of the information content of visible and infrared radiance measurements for cloud microphysical property retrievals over the global oceans, Part I: Liquid clouds, *J. Appl. Meteorol.*, **45**, 20–41.
- Lefer, B. L., R. E. Shetter, S. R. Hall, J. H. Crawford, and J. R. Olson (2003), Impact of clouds and aerosols on photolysis frequencies and photochemistry during TRACE-P: 1. Analysis using radiative transfer and photochemical box models, *J. Geophys. Res.*, **108**(D21), 8821, doi:10.1029/2002JD003171.
- Liou, K. (2002), *An Introduction to Atmospheric Radiation*, Elsevier, New York.
- Long, C. N., and T. P. Ackerman (2000), Identification of clear skies from broadband pyranometer measurements and calculation of downwelling shortwave cloud effects, *J. Geophys. Res.*, **105**(D12), 15,609–15,626.
- Lorente, J., A. Redano, and X. DeCabo (1994), Influence of urban aerosol on spectral solar irradiance, *J. Appl. Meteorol.*, **33**, 406–415.
- Madronich, S. (1993), *Environmental UV Photobiology*, pp. 1–39, Springer, New York.
- McArthur, L. J. B., D. H. Halliwell, O. J. Niebergall, N. T. O'Neill, J. R. Slusser, and C. Wehrli (2003), Field comparison of network Sun photometers, *J. Geophys. Res.*, **108**(D19), 4596, doi:10.1029/2002JD002964.
- McMeeking, G. R., S. M. Kreidenweis, C. M. Carrico, T. Lee, J. L. Collett Jr., and W. C. Malm (2005), Observations of smoke-influenced aerosol during the Yosemite Aerosol Characterization Study: Size distributions and chemical composition, *J. Geophys. Res.*, **110**, D09206, doi:10.1029/2004JD005389.
- Michalsky, J., R. Perez, and R. Stewart (1988), Design and development of a rotating shadowband radiometer solar radiation/daylight network, *Sol. Energy*, **6**, 577–581.
- Nakajima, T., A. Higurashi, K. Kawamoto, and J. Penner (2001), A possible correlation between satellite-derived cloud and aerosol microphysical parameters, *Geophys. Res. Lett.*, **28**(7), 1171–1174.
- Petters, J. L., V. K. Saxena, J. R. Slusser, B. N. Wenny, and S. Madronich (2003), Aerosol single scattering albedo retrieved from measurements of surface UV irradiance and a radiative transfer model, *J. Geophys. Res.*, **108**(D9), 4288, doi:10.1029/2002JD002360.
- Ramanathan, V., P. Crutzen, J. Kiehl, and D. Rosenfeld (2001), Aerosols, climate and the hydrological cycle, *Science*, **294**, 2119–2124.
- Reuder, J., and H. Schwander (1999), Aerosol effects on UV radiation in nonurban regions, *J. Geophys. Res.*, **104**(D4), 4065–4077.
- Rodgers, C. D. (2000), *Inverse Methods For Atmospheric Sounding: Theory and Practice*, World Sci., Hackensack, N. J.
- Schichtel, B. A., K. A. Gebhart, M. G. Barna, and W. C. Malm (2006), Association of air mass transport patterns and particulate sulfur concentrations at Big Bend National Park, Texas, *Atmos. Environ.*, **40**, 992–1006.
- Schuster, G. L., O. Dubovik, and B. N. Holben (2006), Angstrom exponent and bimodal aerosol size distributions, *J. Geophys. Res.*, **111**, D07207, doi:10.1029/2005JD006328.
- Schwander, H., P. Koepke, and A. Ruggaber (1997), Uncertainties in modeled UV irradiances due to limited accuracy and availability of input data, *J. Geophys. Res.*, **102**(D8), 9419–9429.
- Seinfeld, J. H., and S. N. Pandis (1998), *Atmospheric Chemistry and Physics*, John Wiley, Hoboken, N. J.
- Slusser, J., J. Gibson, D. Bigelow, D. Kolinski, W. Mou, G. Koenig, and A. Beaubien (1999), Comparison of column ozone retrievals by use of an UV multifilter rotating shadow-band radiometer with those from Brewer and Dobson spectrophotometers, *Appl. Opt.*, **38**(9), 1543–1551.
- Slusser, J., J. Gibson, D. Bigelow, D. Kolinski, P. Disterhoft, K. Lantz, and A. Beaubien (2000), Langley method of calibrating UV filter radiometers, *J. Geophys. Res.*, **105**(D4), 4841–4849.
- Smirnov, A., B. Holben, T. Eck, O. Dubovik, and I. Slutsker (2000), Cloud-screening and quality control algorithms for the AERONET database, *Remote Sens. Environ.*, **73**, 337–349.
- Stammes, K., S. Tsay, W. Wiscombe, and K. Jayaweera (1988), Numerically stable algorithm for discrete-ordinate-method radiative transfer in multiple scattering and emitting layered media, *Appl. Opt.*, **27**, 2502–2509.
- Stephens, G. L. (1994), *Remote Sensing of the Lower Atmosphere*, Oxford Univ. Press, New York.
- Suzuki, K., T. Nakajima, A. Numaguti, T. Takemura, K. Kawamoto, and A. Higurashi (2004), A study of the aerosol effect on a cloud field with simultaneous use of GCM modeling and satellite observation, *J. Atmos. Sci.*, **61**, 179–194.
- Toon, O., C. McKay, and T. Ackerman (1989), Rapid calculation of radiative heating rates and photodissociation rates in inhomogeneous multiple scattering atmospheres, *J. Geophys. Res.*, **94**, 16,287–16,301.
- Wenny, B., J. Schafer, J. DeLuisi, V. Saxena, W. Barnard, I. Petropavlovskikh, and A. Vergamini (1998), A study of regional aerosol radiative properties and effects on ultraviolet-B radiation, *J. Geophys. Res.*, **103**, 17,083–17,097.
- Wenny, B., V. Saxena, and J. Frederick (2001), Aerosol optical depth measurements and their impact on surface levels of ultraviolet-B radiation, *J. Geophys. Res.*, **106**(D15), 17,311–17,319.
- Wetzel, M. A., G. E. Shaw, J. R. Slusser, R. D. Borys, and C. F. Cahill (2003), Physical, chemical, and ultraviolet radiative characteristics of aerosol in central Alaska, *J. Geophys. Res.*, **108**(D14), 4418, doi:10.1029/2002JD003208.

J. R. Slusser and T. E. Taylor, USDA UV Monitoring and Research Program, Colorado State University, Fort Collins, CO 80521, USA. (ttaylor@uvb.nrel.colostate.edu)

C. D. Goering, T. S. L'Ecuyer, and G. L. Stephens, Department of Atmospheric Science, Colorado State University, Fort Collins, CO 80523, USA.